UNIVERSITY OF HELSINKI

https://helda.helsinki.fi

Microphysical Properties of Snow and Their Link to Z(e) -S Relations during BAECC 2014

von Lerber, Annakaisa; Moisseev, Dmitri; Bliven, Larry F.; Petersen, Walter; Harri, Ari-Matti ...

2017-06
American Meteorological Society
http://hdl.handle.net/10138/308167
von Lerber, A, Moisseev, D, Bliven, L F, Petersen, W, Harri, A-M & Chandrasekar, V 2017, 'Microphysical Properties of Snow and Their Link to Z(e)-S Relations during BAECC 2014', Journal of Applied Meteorology and Climatology, vol. 56, no. 6, pp. 1561-1582. https://doi.org/10.1175/JAMC-D-16-0379.1

Downloaded from Helda, University of Helsinki institutional repository. https://helda.helsinki.fi
This is an electronic reprint of the original article.
This reprint may differ from the original in pagination and typographic detail.
Please cite the original version.

Microphysical Properties of Snow and Their Link to Z_e–S Relations during BAECC 2014

ANNAKAISA VON LERBER,[a,b] DMITRI MOISSEEV,[c,a] LARRY F. BLIVEN,[d] WALTER PETERSEN,[e] ARI-MATTI HARRI,[a] AND V. CHANDRASEKAR[f,a,c]

[a] *Finnish Meteorological Institute, Helsinki, Finland*
[b] *School of Electrical Engineering, Aalto University, Espoo, Finland*
[c] *Department of Physics, University of Helsinki, Helsinki, Finland*
[d] *NASA Goddard Space Flight Center, Wallops Flight Facility, Wallops Island, Virginia*
[e] *NASA Marshall Space Flight Center, Earth Science Office, Huntsville, Alabama*
[f] *Colorado State University, Fort Collins, Colorado*

(Manuscript received 1 December 2016, in final form 16 March 2017)

ABSTRACT

This study uses snow events from the Biogenic Aerosols–Effects on Clouds and Climate (BAECC) 2014 campaign to investigate the connection between properties of snow and radar observations. The general hydrodynamic theory is applied to video-disdrometer measurements to retrieve masses of falling ice particles. Errors associated with the observation geometry and the measured particle size distribution (PSD) are addressed by devising a simple correction procedure. The value of the correction factor is determined by comparison of the retrieved precipitation accumulation with weighing-gauge measurements. Derived mass–dimensional relations are represented in the power-law form $m = a_m D^{b_m}$. It is shown that the retrieved prefactor a_m and exponent b_m react to changes in prevailing microphysical processes. From the derived microphysical properties, event-specific relations between the equivalent reflectivity factor Z_e and snowfall precipitation rate S ($Z_e = a_{zs}S^{b_{zs}}$) are determined. For the studied events, the prefactor of the Z_e–S relation varied between 53 and 782 and the exponent was in the range of 1.19–1.61. The dependence of the factors a_{zs} and b_{zs} on the $m(D)$ relation and PSD are investigated. The exponent of the Z_e–S relation mainly depends on the exponent of the $m(D)$ relation, whereas the prefactor a_{zs} depends on both the intercept parameter N_0 of the PSD and the prefactors of the $m(D)$ and $v(D)$ relations. Changes in a_{zs} for a given N_0 are shown to be linked to changes in liquid water path, which can be considered to be a proxy for degree of riming.

1. Introduction

Natural variability of physical characteristics of ice particles is large (Magono and Nakamura 1965). Particle properties are driven by various growth processes, that is, diffusional growth, riming, and aggregation, occurring separately or simultaneously. As a result, microphysical properties of snowfall can vary on a temporal scale of a few minutes. Therefore the parameterization of a relation between radar observations and liquid-equivalent snowfall rate is challenging and is a topic of continuous interest since the pioneering studies of, for example, Marshall and Gunn (1952) and Langille and Thain (1951). Detailed in situ observations of snowfall microphysics are needed for validation of physical assumptions used in space-based (Turk et al. 2011; Skofronick-Jackson et al. 2013; Wood et al. 2015) and ground-based (Gunn and Marshall 1958; Sekhon and Srivastava 1970; Ohtake and Hemni 1970; Fujiyoshi et al. 1990; Rasmussen et al. 2003; Huang et al. 2010; Lim et al. 2013; Huang et al. 2015) remote sensing precipitation retrieval algorithms as well as for verification and improvement of microphysical parameterizations utilized in numerical weather prediction models (e.g., Thompson et al. 2004; Harrington et al. 2013; Morrison and Milbrandt 2015).

In the past, properties of individual particles were recorded manually (see, e.g., Nakaya and Tereda 1935; Langleben 1954; Magono and Nakamura 1965; Zikmunda and Vali 1972; Zikmunda 1972; Kajikawa 1972; Locatelli and Hobbs 1974). Because this process is time consuming, only a limited number of ice particles were typically sampled. For example, Locatelli and Hobbs (1974) report observations from 9 to 58 samples of each particle type.

Corresponding author: Annakaisa von Lerber, annakaisa.von.lerber@fmi.fi

DOI: 10.1175/JAMC-D-16-0379.1

© 2017 American Meteorological Society. For information regarding reuse of this content and general copyright information, consult the AMS Copyright Policy (www.ametsoc.org/PUBSReuseLicenses).

Automatic observations of snowfall using optical disdrometers, such as the Particle Video Imager/Particle Imaging Package (PVI/PIP; Newman et al. 2009), 2D video disdrometer (2DVD; Kruger and Krajewski 2002; Schönhuber et al. 2007), Hydrometeor Velocity and Shape Detector (HVSD; Barthazy et al. 2004), Particle Size and Velocity (Parsivel; Löffler-Mang and Joss 2000; Löffler-Mang and Blahak 2001), or Multi-Angle Snowflake Camera (MASC; Garrett et al. 2012), offer a possibility to document properties of ice particles continuously and on temporal scales starting from a few minutes to covering whole snow storms. These observations typically include particle size, fall velocity, particle size distribution (PSD), and some description of a particle shape. The size and shape of a particle are defined from 2D images on a single projection plane (e.g., by PVI/PIP and HVSD), or on two orthogonal planes (e.g., by 2DVD), or on three planes separated by 36° (e.g., by MASC). To retrieve masses of falling snow particles from such measurements, for example, the mass–dimensional relation $m(D)$, three methods have been applied in the past (Heymsfield et al. 2004). First, data from an optical disdrometer are combined with observations from other instruments (e.g., Muramoto et al. 1995; Heymsfield et al. 2004; Brandes et al. 2007; Huang et al. 2010; Wood et al. 2014; Tiira et al. 2016). Second, the general hydrodynamic theory (Böhm 1989) can be used in connecting particle terminal velocity and shape (e.g., Hanesch 1999; Szyrmer and Zawadzki 2010; Huang et al. 2015). The third method is applicable for single ice crystals with regular geometrical structure, where mass can be estimated from the projected cross-sectional area (Heymsfield et al. 2004). All methods are well represented in the literature. Muramoto et al. (1995) defined the density–dimensional relation by combining side-viewing camera images of snow particles with the weight of the ensemble of particles measured on an electronic balance. Heymsfield et al. (2004) analyzed PSD measured with airborne particle spectrometers simultaneously with direct measurements of ice water content in deriving the $m(D)$ relations. Brandes et al. (2007) combined the PSD and velocity measured with 2DVD and weighing-gauge-measured liquid water equivalent (LWE) accumulation. In a similar way, Tiira et al. (2016) merged measurements of PIP and gauges to retrieve a relation between ensemble mean snow density and particle median volume diameter. Huang et al. (2010) have minimized the difference between equivalent reflectivity factor measured by a C-band weather radar and derived from the 2DVD observations of PSD by adjusting three parameters: coefficients of density–dimensional relation and an adjustment parameter for correcting wind-induced errors in PSD measurements. As a result they have derived density–dimensional relations for 11 snowfall periods. Wood et al. (2014) have constructed a Bayesian optimal estimation retrieval process, to jointly derive $m(D)$ relations and horizontally projected area–dimensional $A(D)$ relations by constraining the optimization using equivalent radar reflectivity factor, PSD, snowfall rate, and velocity–dimensional [$v(D)$] observations.

In this study the focus is on obtaining automatic and reliable measurements of $v(D)$ and retrievals of $m(D)$ relations on temporal scales of few minutes to verify microphysical processes observed using remote sensing instruments. The dimension D in the relations is the maximum diameter from a single projection. The proposed retrieval procedure is applied to 10 snow events recorded during the Biogenic Aerosols–Effects on Clouds and Climate (BAECC) 2014 campaign (Petäjä et al. 2016). The main instrument used in this study is the video disdrometer PIP (Tiira et al. 2016; Newman et al. 2009). The mass of ice particles is retrieved using hydrodynamic theory (Böhm 1989; Mitchell and Heymsfield 2005; Khvorostyanov and Curry 2002, 2005). Given the uncertainty of determining ice particle shapes from single-plane images (Wood et al. 2013), an estimate of the difference between the observed and true particle dimensions is proposed. Also, sampling limitations of PSD are considered together with the particle-dimension adjustment in a simple correction procedure. This method adjusts the estimate of particle mass such that the retrieved precipitation accumulation from PIP matches observations from the weighing gauge.

Given the derived relations of $v(D)$ and $m(D)$ and the measured PSD, the precipitation rate S and equivalent reflectivity factor Z_e are determined. For each of the studied snow events, the Z_e–S relation in power-law format $Z_e = a_{zs}S^{b_{zs}}$ is found. These relations are then applied to weather-radar measurements from the Finnish Meteorological Institute (FMI) Ikaalinen site (Saltikoff et al. 2010) and are compared with the gauges in the vicinity of the radar. The dependence of the Z_e–S factors on $m(D)$ relation and PSD is investigated. Also the connection between measured liquid water path (LWP) and changes in prefactor a_{zs} for a given N_0 (intercept parameter of PSD) are shown.

2. Measurement site and instruments

a. Measurement site

The PIP and two OTT Hydromet GmbH Pluvio^2 weighing gauges are used in this study. These instruments are deployed at the measurement site as a part of the National Aeronautics and Space Administration (NASA) Global Precipitation Measurement ground validation (GPM GV) program. In January of 2014 they

were installed at the University of Helsinki Hyytiälä Forestry Field Station in southern Finland (61.845°N, 24.287°E; above 150 m MSL) and were used also during the snowfall intensive observation period (IOP) of the BAECC field campaign snowfall measurement experiment (SNEX) from 1 February through 30 April 2014 (Petäjä et al. 2016). BAECC is a joint effort among the University of Helsinki, the Finnish Meteorological Institute, and the U.S. Department of Energy Atmospheric Radiation Measurement (ARM) program. The IOP, known as BAECC SNEX, focused on microphysical observations of snow, and the measurement setup was designed while considering the challenges of snowfall measurements (Rasmussen et al. 2012). The instruments were placed in the middle of a forest clearing sheltered by the surrounding trees, with the closest trees located at about 20-m distance. The wind effects were studied by deploying part of the instrumentation inside the wind fence similar to World Meteorological Organization standard ''double fence intercomparison reference'' (DFIR) wind protection (Goodison et al. 1998) and duplicating the measurement setup outside the fence. The wind conditions were measured with 3D anemometers at the height of the instruments both inside the DFIR fence and outside on the field.

b. *Instruments*

1) Particle Imaging Package

The video disdrometer known as PIP is the successor of PVI (Newman et al. 2009), with a higher frame rate (380 frames per second) and with a new particle-tracking software enabling measurements of particle fall velocities. The measurement principle is the same—the 2D grayscale video images are recorded as particles fall between a light source and a charge-coupled-device camera. Because of the high frame rate, multiple observations of a single particle are recorded, and the fall velocity is retrieved. The distance between the lamp and the camera is ~2 m. The field of view (48 mm × 64 mm) of PIP is larger than that of its predecessor, and pixel size is 0.1 mm × 0.1 mm. The detection algorithm in PIP is similar to that of PVI (Newman et al. 2009). In the current algorithm, particles that are smaller than 14 pixels are rejected, effectively meaning that particles smaller than a disk-equivalent diameter D_{deq} of approximately 0.2 mm are not observed, D_{deq} being the diameter of a disk with the same area of the particle image. The measurement volume of PIP is defined by the field of view and the depth of field. Particles that fall partly outside the volume are excluded. The standard error in observed particle size has been estimated to be 18% (Newman et al. 2009). The measurement volume of PVI/PIP is not enclosed. Therefore, in calm to moderate wind conditions the expected effects of the instrument on measurements of particle PSD (Nešpor et al. 2000) are minimal.

The 1-min PSD of the recorded particles is given as a function of D_{deq}. Data used in the study are recorded and analyzed with PIP software release 1308. In this software version, the measured D_{deq}s are divided into 105 bins (with center ranging from 0.125 to 25.875 mm), and one bin is for all particles larger than 25.875 mm. Velocity observations are also given as a function of D_{deq}. If there are fewer than three measurements of the particle or the velocity value is less than 0.5 m s^{-1}, then the particle is excluded from analysis. The fall velocity threshold of 0.5 m s^{-1} is set in the software version 1308; it is removed from later versions. The threshold limits the detection of small particles (approximately at $D_{\mathrm{deq}} < 0.20$ mm) and affects the measured PSD. The induced error in precipitation rate because of the small particle truncation in PSD is discussed later on in section 3c.

The particle-shape data are processed with National Instruments Corporation ''IMAQ'' (image acquisition) software. The preselected output from IMAQ retrievals include in addition to D_{deq}, for example, total area as an area of shadowed pixels A_{tot}, bounding-box dimensions, and particle orientation with respect to the horizontal axis. An ellipse, with a major diameter D_{maj} and a minor diameter D_{min}, is fitted inside a given bounding box with a given orientation. A schematic image of fitting is shown in Fig. 1d, where W describes the maximum width and H is the maximum height. Note that the major diameter $D_{\mathrm{max}} = D_{\mathrm{maj}}$ and minor diameter D_{min} are not necessarily defining a circumscribing ellipse; some parts of a particle could lie outside the ellipse boundary. Because of this, the area ratio A_r that is used in this study is defined as the measured total area of a particle divided by the area of a circumscribing circle, that is, $A_r = A_{\mathrm{tot}}/(\pi D_{\mathrm{max}}^2/4)$, and is limited to be smaller than or equal to 1. Given that each particle is observed several times, for every particle, mean values of the multiple observations of D_{deq}, fall velocity v, total area A_{tot}, and both minor D_{min} and major D_{maj} diameters are calculated. As an exception, the largest observed dimension D_{max} of a particle, which is used in the $m(D)$-relations retrieval, is defined as the maximum value of the observed D_{maj} values. For each studied snow event, the linear ratio between the observed D_{max} and the D_{deq} is determined; the scale factors of the linear relations were deviating among 1.20–1.51, and the mean value was 1.38. The scale

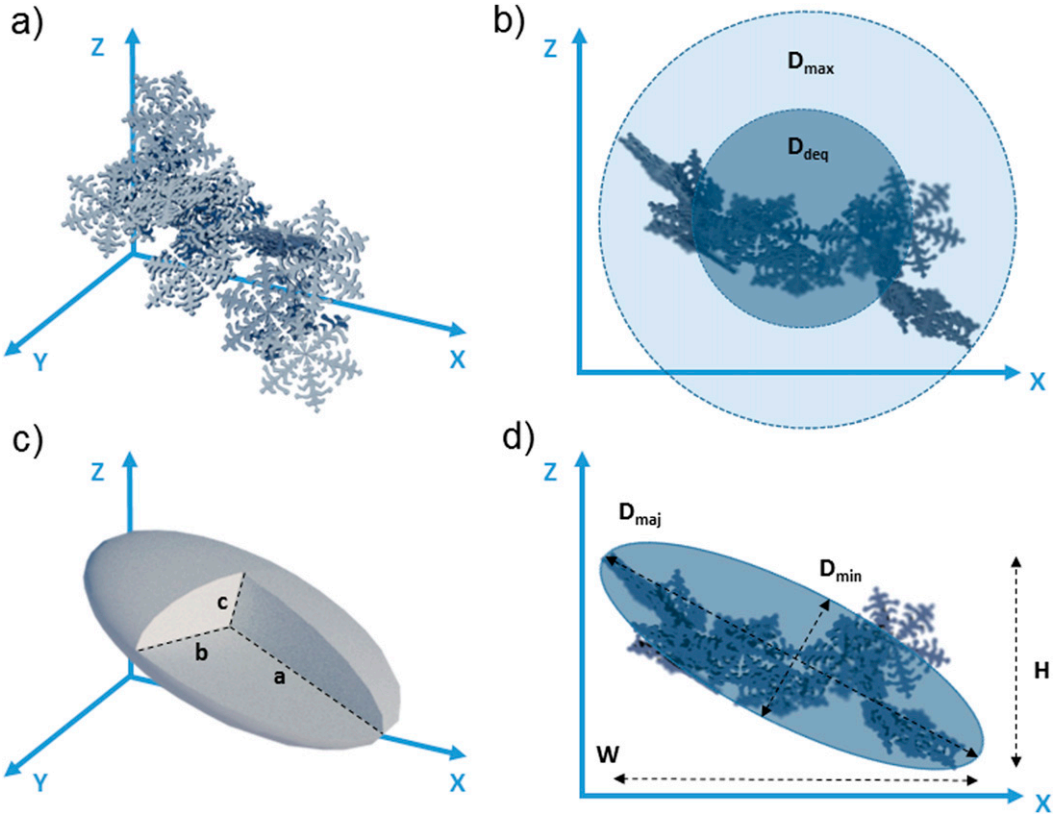


FIG. 1. Schematic image describing the projection of the video disdrometer and the used dimensions. (a) Schematic image of snowflake and (b) plane projection in side view (x–z) of the particle with D_{deq} and D_{max}. (c) Snowflake modeled as ellipsoid with axes a, b, and c, and (d) plane projection in side view of the ellipsoid with definitions of the fitted ellipse D_{maj} and D_{min} and the maximum width W and height H.

factors are used to convert D_{deq} to observed D_{max}. The conversion of the observed D_{max} to a proxy of a true D_{max} is discussed in section 3b.

2) PRECIPITATION GAUGES

In addition to PIP, two weighing gauges are located at the Hyytiälä measurement site (Petäjä et al. 2016). The OTT Pluvio^2 200, with an orifice of 200 cm^2, is located on the platform inside the double wind fence; in addition, the gauge has a Tretyakov wind shield. The Pluvio^2 400, with an orifice of 400 cm^2, is placed on the field about 20 m from the double wind fence and from PIP. It has both Tretyakov and Alter wind shields. The Pluvio^2 200 is another ground-based precipitation instrument that is used in the study because it is expected to have less precipitation undercatchment. It was, however, observed (Tiira et al. 2016) that the discrepancy between gauge precipitation accumulation observations is not large; it varies between 1% and 15%. In this study the instrument output of the measured filtered bucket content in millimeters is used; it is recorded every minute and is accumulated over 5-min time periods.

The precipitation gauges of the FMI automatic weather stations are used in the validation of radar-based precipitation estimates. These gauges are also OTT Pluvio^2 400 models. The gauges are sheltered with Alter wind shields, and sensor orifices are set at 1.5 m above ground level.

3) DUAL-POLARIZATION DOPPLER WEATHER RADAR

The FMI operational dual-polarization Doppler weather radar employed in this study is located in Ikaalinen, approximately 64 km west from Hyytiälä. It is performing plan position indicator (PPI) scans at the lowest elevation angle of 0.3° every 5 min. The operating frequency is 5.5 GHz, with a beamwidth of 1°. The minimum detectable Z_e is −48 dBZ at 1-km range (Saltikoff et al. 2010). To compare the radar-based estimations of accumulated LWE with the gauge measurements, the derived Z_e–S relations are applied to the PPI scans. Because the lowest elevation angle is utilized, clutter and beam blockages cause loss in the signal in some areas. These losses are examined with a stationary statistical ground-clutter map

(Lakshmanan et al. 2012). The clutter map is defined from clear-air echoes during the time period of 1 December 2014–1 February 2015. With the threshold value set for observing persistent echo over −5 dB or more than 60% of the time for the elevation angle of 0.3°, the area surrounding the Ikaalinen radar over a distance of approximately 20 km is partly contaminated with ground clutter, and the wind farm northwest from the Ikaalinen radar is very clearly seen. Also, in examining the snow-accumulation periods of the BAECC campaign, the partial beam blockages can be identified to the five azimuthal directions. When comparing the radar-estimated and gauge-measured LWE accumulations, none of the selected FMI operational gauges is located in the direction of the partial beam blockages, nor are they at locations of the clutter-contaminated radar bins. Therefore, the snowfall-rate values are not expected to have errors because of the clutter, but these can be seen as artifacts in the accumulation maps.

4) TWO-CHANNEL MICROWAVE RADIOMETER

Observations of the LWP (Cadeddu 2014) that are retrieved from the ARM second ARM mobile facility (AMF2) two-channel microwave radiometer (MWR) measurements are utilized in this study as a proxy for riming. The MWR is located on the instrumentation field 20 m away from PIP.

3. Methods to derive $m(D)$ and $Z_e(S)$ relations

a. The mass derived with hydrodynamic theory

A hydrometeor falling at the terminal velocity in still air can be considered to be a particle moving through a fluid. In this case, the equation of motion is determined from equilibrium of forces acting on the particle, that is, drag, buoyancy, and gravity. Böhm (1989) applied the boundary layer theory (List and Schemenauer 1971; Abraham 1970) and defined a semiempirical dependence between the Reynolds number R_e and the Best number X to describe the terminal fall velocity of a hydrometeor as a function of its mass and area projected to the airflow. This method, or a variation of it, is widely used either to retrieve the terminal fall velocity or, inversely, to retrieve the mass of hydrometeors (e.g., Mitchell 1996; Hanesch 1999; Khvorostyanov and Curry 2002, 2005; Mitchell and Heymsfield 2005; Heymsfield and Westbrook 2010; Szyrmer and Zawadzki 2010; Wood et al. 2014; Huang et al. 2015). The Reynolds number can be stated as

$$R_e = \frac{\delta_0^2}{4}\left[\left(1+\frac{4X^{1/2}}{\delta_0^2 C_0^{1/2}}\right)^{1/2}-1\right]^2, \tag{1}$$

or, vice versa, the Best number can be written as

$$X = \left(\frac{\delta_0^2 C_0^{1/2}}{4}\left\{\left[\frac{(4R_e)^{1/2}}{\delta_0}+1\right]^2-1\right\}\right)^2, \tag{2}$$

where the heuristic coefficients are the boundary layer thickness $\delta_0 = 5.83$ and the pressure drag coefficient $C_0 = 0.6$ (Böhm 1989). The Best number by definition is $X = C_d R_e^2$ (Pruppacher and Klett 1997) and can be expressed without dependence on fall velocity as, for example (Mitchell 1996),

$$X = \frac{2mg\rho_a D_c^2}{\eta^2 A_e}, \tag{3}$$

where g is the gravitational acceleration, m is the particle mass, ρ_a is the air density, D_c is the characteristic length of a particle, η is the dynamic viscosity, and A_e is the true effective particle area (containing only area of the ice parts) normal to the flow.

The particle mass can be estimated by first computing the Reynolds number

$$R_e = \upsilon D_c \rho_a/\eta, \tag{4}$$

where υ is the measured particle terminal fall velocity. Then by substituting R_e into Eq. (2) and obtaining the Best number X and solving for mass from Eq. (3)

$$m = \frac{\pi\eta^2 X}{8g\rho_a}\left(\frac{A_e}{A_\perp}\right)^{1/4}, \tag{5}$$

where it is assumed that the drag coefficient of a snow particle C_{de} is related to the drag coefficient of an equivalent disk C_d as (Böhm 1989)

$$C_{de}/C_d = (A_\perp/A_e)^{3/4}, \tag{6}$$

with $A_\perp$ as the circumscribed area normal to the flow. Böhm (1989) defines $A_\perp$ as the area of the smallest circle or ellipse, which contains all of the A_e. Often, as in this study, D_c is described as the maximum dimension in Eq. (4) and the circumscribing circle area is described as $A_\perp$ (Mitchell 1996; Khvorostyanov and Curry 2005; Mitchell and Heymsfield 2005; Heymsfield and Westbrook 2010; Szyrmer and Zawadzki 2010). Nevertheless, PIP observes particles from a side, not normal to the flow, as discussed in more detail in section 3b.

Mitchell and Heymsfield (2005) modified the original derivation of the $R_e(X)$ relation Eq. (1) to improve estimates of fall velocities for aggregates,

$$R_e = \frac{\delta_0^2}{4}\left[\left(1+\frac{4X^{1/2}}{\delta_0^2 C_0^{1/2}}\right)^{1/2}-1\right]^2 - a_0 X^{b_0}, \tag{7}$$

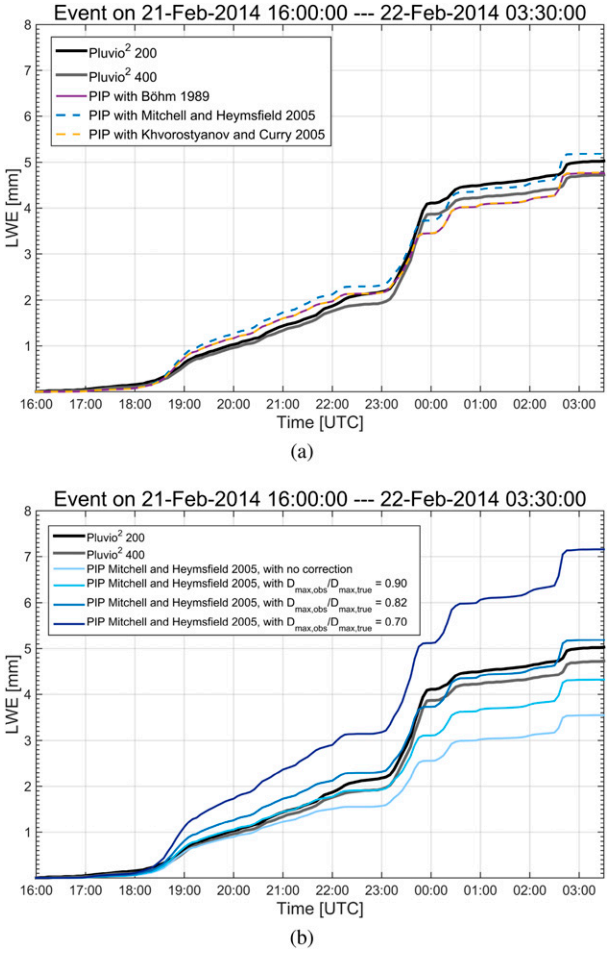


FIG. 2. An example of the sensitivity of the accumulated estimate of LWE to (a) selected versions of the hydrodynamic theory and (b) selected correction of $D_{\mathrm{max,obs}}$ with respect to $D_{\mathrm{max,true}}$.

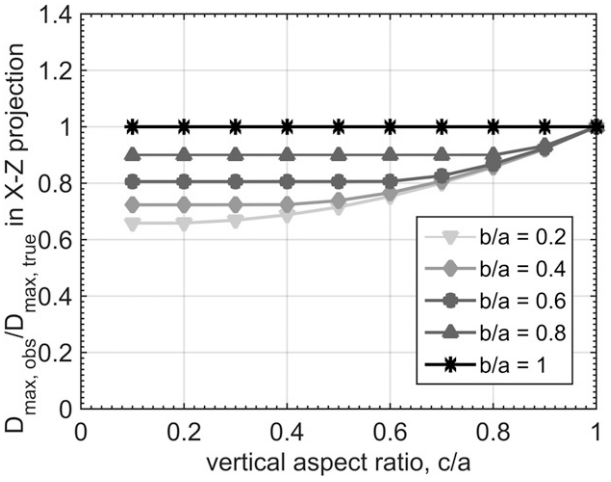


FIG. 3. The ratio of maximum observed diameter from the side with respect to the true maximum diameter computed by averaging projections of a rotating ellipsoid with axes defined in Fig. 1c.

where the second term accounts for the dilation of the boundary layer thickness and increase of effective area projected to the flow, with coefficients $a_0 = 1.7 \times 10^{-3}$ and $b_0 = 0.8$. Szyrmer and Zawadzki (2010) derived an eighth-order polynomial fit for proposed relations of $X(R_e)$ of Mitchell and Heymsfield (2005) and Khvorostyanov and Curry (2005). The two polynomial fits and the first version from Böhm (1989) without turbulence correction are implemented in this study. The derived $m(D)$ relations using different methods are compared by estimating accumulated LWE for each event (an example figure of the version differences is shown in Fig. 2a). The differences are small, deviating between −0.2% and 9.1%. Because all three methods produce similar results, the version presented by Mitchell and Heymsfield (2005) is utilized in this study.

b. *Estimating uncertainty in particle dimensions*

All of the ground-based disdrometers observe falling particles from the side. For the hydrodynamic calculations, the particle dimensions projected to the flow are needed. There are two aspects of the viewing geometry that need to be addressed before particle masses can be retrieved. First, the particle dimensions estimated from one projection are not necessarily identical to the true dimensions. Second, a relation between a particle area observed from the side and one needed for the mass retrieval has to be established.

To study a relation between observed and true particle dimensions, an approach similar to that of Wood et al. (2013) and Tiira et al. (2016) has been adopted. The idealized shape of an ellipsoid is used to determine the correction factor between the observed maximum diameter $D_{\mathrm{max,obs}}$ and a true maximum diameter $D_{\mathrm{max,true}}$. The ellipsoid is described by three axes, and the axes are shown in Fig. 1c. Because the observed dimensions depend on particle orientation, ellipsoid orientations followed those of snowflakes, that is, a uniform distribution of azimuth angles and a Gaussian distribution of canting angles with a standard deviation of 9° as suggested by Matrosov et al. (2005). The values of assumed aspect ratios are given in Fig. 3. For each set of aspect ratios, $D_{\mathrm{max,obs}}$ defined on a single projection plane (X–Z) is calculated and is averaged over all orientations (~87 000). The results of these calculations are shown in Fig. 3 and are in line with the findings of Wood et al. (2013). The ratio linking $D_{\mathrm{max,obs}}$ and $D_{\mathrm{max,true}}$ depends more on the horizontal aspect ratio (b/a) than on the vertical aspect ratio (c/a). The ratios have also been computed with a larger standard deviation up to 39° (Garrett et al. 2015), and the changes to the results obtained with the standard deviation of 9°, are hardly noticeable. Hence it can be concluded that the

ratio is more sensitive to the particle shape than to the canting angle (Wood et al. 2013).

An example of the sensitivity of the mass estimate to the particle dimension correction is depicted in Fig. 2b. The diameter $D_{\mathrm{max,obs}}$ in Eq. (4) is converted to $D_{\mathrm{max,true}}$ with a single ratio value for the whole event. The chosen correction has a larger effect on the mass estimate than the different methods of the hydrodynamic theory. Here the used maximum correction increases the observed diameters by 42% (ratio value of 0.7), and this can lead to variations of up to 102% in the estimated accumulated LWE depending on the snowfall case.

In this study, the adopted correction is applied to Eq. (4) by multiplying the diameter and the value is determined by comparing estimated accumulated LWE with gauge-measured accumulation. There is also another limitation, which is caused by the viewing geometry and can be attributed to the selected correction value. Here it is assumed that the particle porosity is independent of the viewing angle (Szyrmer and Zawadzki 2010). In the case of crystals and highly oblate particles, however, this approximation may not be valid. For these particles, area ratio normal to flow is significantly higher than that observed from the side. The effect of area ratio to the mass estimate is stated in Eq. (5). Examining the correction factor that is based on the ratio of the observed diameter to the true maximum diameter, by changing the value from 0.82 to 0.70, is equal to an increase of 28% in mass, which can be reached also by assuming the area ratio of particles to be closer to 1 in Eq. (5). In another words, in cases in which the single correction factor is chosen to be 0.7 and is applied to Eq. (4), and particles seem to be generally more oblate, the prevailing snow type can be estimated also with correction factor of 0.82 assuming area ratio of particles to be close to 1. Both corrections produce the same estimated accumulated LWE. Therefore, given the observations used in this study, it is not possible and not really needed to separate the two limitations of the viewing geometry. A single correction factor can be used to address both aspects.

c. *Deriving time series of $m(D)$ and Z_e–S relations*

Time series of PSD parameters, $m(D)$, and Z_e–S relation coefficients are retrieved every 5 min. This time period is believed to be short enough to detect changes in the prevailing particle types but sufficiently long to have enough observations for the retrievals. Before averaging over 5 min, the recorded 1-min PSDs are filtered to exclude spurious measurements of large particles (Tiira et al. 2016; Leinonen et al. 2012). All parameters derived from PSD measurements are expressed as functions of D_{deq}. The median volume diameter $D_{\mathrm{deq,0}}$ and total particle concentration N_T are calculated on the basis of the 5-min-averaged PSD and estimated using standard methods (see, e.g., Leinonen et al. 2012). The amount of particles that are typically observed during the 5-min time period is around 10^3, varying from 62 to 31 400. It is assumed that in general the sample size is large enough for the accuracy of moment estimators (Smith and Kliche 2005).

As stated in the section 2b, PIP velocity observations are given as functions of D_{deq}. To be comparable with other studies, both $m(D)$ and $v(D)$ relations are expressed as functions of true D_{max}. To achieve this, the disk-equivalent diameter D_{deq} is scaled with the event-specified scaling factor as described in section 2b and also applying the dimension correction between $D_{\mathrm{max,obs}}$ and $D_{\mathrm{max,true}}$. For the sake of simplicity, hereinafter D stands for our proxy of true maximum diameter $D_{\mathrm{max,true}}$ and the relations are stated as $m(D)$ and $v(D)$.

To derive $v(D)$ relations, a linear-regression fit in log space is performed, as described in detail in Tiira et al. (2016). The fitting process is found to be stable if a minimum limit of 30 particle records is chosen. An additional constraint of limiting the exponent b_v to be larger than zero is also added. The mean error of the fits is calculated from the sum of squared residuals for all of the 5-min fits of all studied cases to be 0.021 m s^{-1}, which, with respect to mean velocity value, is approximately 2%. The mean standard error of the coefficients for a_v is 0.012 m s^{-1} (1.5% with respect to mean value of 0.77 m s^{-1}) and for b_v is 0.022 (9% with respect to mean value of 0.25). In the time periods in for which several particle types with very different properties are present a single power-law fit may not necessarily be representative. At this time, no particle classification is performed, and bulk properties potentially representing several particle types are derived.

From the velocity observations, time series of $m(D)$ relation coefficients, assuming that the relation can be expressed as a power law $m(D) = a_m D^{b_m}$, are retrieved. The mass estimate with the unitless correction factor (explained in section 3b) is computed for all particles observed during the time period, by applying Eqs. (4)–(7). The power-law coefficients are derived by performing the linear regression in log scale. In a way that is similar to that of velocity fits, the mean error of the fits is calculated from the sum of squared residuals for all the 5-min fits of all studied cases. The error is estimated to be 9.38×10^{-7} g and, in percentages related to mean mass, to be 0.1%. The mean standard error of the coefficients for a_m is 0.002 g cm$^{-b_m}$ (25% with respect to the mean value of 0.0083 g cm$^{-b_m}$), and for b_m it is 0.095 (5% with respect to the mean value of 2.11).

The observed PSDs, fitted $v(D)$ relation, and retrieved $m(D)$ relation are combined to calculate the bulk properties such as liquid-equivalent precipitation rate given in millimeters per hour,

$$S(t) = \frac{3.6 \times 10^3}{\rho_w} \int_{d_{\min}}^{d_{\max}} m(D,t) v(D,t) N(D_{\text{deq}}, t)\, dD_{\text{deq}}, \tag{8}$$

and precipitation accumulation G in millimeters,

$$G = \frac{1}{\rho_w} \int_{t}^{t+\Delta t} \int_{d_{\min}}^{d_{\max}} m(D,t) v(D,t) N(D_{\text{deq}}, t)\, dD_{\text{deq}}\, dt, \tag{9}$$

where the lower limit of the integral $d_{\min}$ is the minimum observable particle size, which is 0.28 mm for the PIP with BAECC data, and the upper limit $d_{\max}$ is the maximum observed dimension. Tiira et al. (2016) have studied the impact of small-particle PSD truncation on the precipitation accumulation estimation and found that it is a function of median volume diameter $D_{\text{deq},0}$. For $D_{\text{deq},0}$ values that are smaller than 1 mm, the precipitation rate will be underestimated by 10%–20%. For larger $D_{\text{deq},0}$ values, this bias is smaller than 5%.

To derive Z_e–S relations, which can be applied to the measurements from the FMI C-band weather radar, the equivalent reflectivity factor is computed from the observed PSD and the retrieved $m(D)$ relations using the Rayleigh-scattering approximation (Atlas et al. 1953). The dielectric constant of snowflakes $|K_s|$ is computed by the two-phased Maxwell Garnett mixing formula of a mixture of ice and air (Sihvola 1999). The mixing formula provides $|K_s|$ as a function of snowflake density ρ_s as

$$|K_s|^2 \approx \frac{\rho_s^2}{\rho_{\text{ice}}^2} |K_{\text{ice}}|^2$$

(Bringi and Chandrasekar 2001). The equivalent reflectivity factor of spherical particles is given then as (Battan 1973)

$$Z_e(t) = \frac{36 \times 10^6}{\pi^2 \rho_{\text{ice}}^2} \frac{|K_{\text{ice}}|^2}{|K_w|^2} \int_{d_{\min}}^{d_{\max}} m(D,t)^2 N(D_{\text{deq}}, t)\, dD_{\text{deq}}, \tag{10}$$

where at C band dielectric constant values of ice $|K_{\text{ice}}|^2 = 0.17$ and water $|K_w|^2 = 0.93$ are used. The density of ice is $\rho_{\text{ice}} = 0.917\ \text{g cm}^{-3}$. In general at C band it is assumed that the shape of the particles has little effect on backscattered reflectivity. For spheroids, the reflectivity factor can be described as (Bringi and Chandrasekar 2001)

$$Z_e(t) = \frac{36 \times 10^6}{\pi^2 \rho_{\text{ice}}^2} \frac{|K_{\text{ice}}|^2}{|K_w|^2} \frac{1}{\left|1 + \frac{\delta_v K_{\text{ice}}}{2}(1 - 3\lambda_z)\right|^2} \int_{d_{\min}}^{d_{\max}} m(D,t)^2 N(D_{\text{deq}}, t)\, dD_{\text{deq}}, \tag{11}$$

where δ_v is the volume fraction of ice inclusions in snow in the Maxwell Garnett mixing formula and λ_z is the depolarization factor of the oblate spheroid. For spheres, $\lambda_z = 1/3$, and thus Eqs. (10) and (11) are equal. For plates, $\lambda_z = 1$, which is presenting the highest value for the term $1 - 3\lambda_z$, and the increase of reflectivity factor will be around 10%, equal to an increase of 0.4 dBZ, when assuming $\delta_v = 0.1$. Hence the uncertainty in the prefactor of the Z_e–S relation induced from the shape of the snow particles is smaller than 10%.

4. Results and discussion of the studied snow cases during BAECC SNEX 2014

Ten snow events that took place during the BAECC SNEX campaign were selected for this study, and the environmental conditions are summarized in Table 1. The winter of 2013/14 was mild. The average temperature ranged from −4° to −2°C, which was approximately 3°C warmer than that of the statistical observation period of 1981–2010 (FMI climateservice 2014). For the majority of the studied snowfall events, the temperature was between −4° and 0°C with the exception of 31 January–1 February, on which dates the measured temperature was close to −8°C. The selected events are restricted to the time periods for which the temperatures were below 0°C as measured by the ARM surface meteorological station (Kyrouac and Holdridge 2014). The events for which the temperatures were just below 0°C during the whole event were rejected because the onset of melting could not be ruled out. The average and the maximum wind speeds for each event are derived from the recorded 60-s-average measurements of a Gill Instruments, Ltd., anemometer located on the measurement field at a height of 1.2 m and are shown in Table 1. These wind measurements describe wind conditions at the height of the instruments.

a. The diameter correction factor

For the retrieval of the $m(D)$ relations, the diameter correction factor has to be computed as described in

TABLE 1. Studied snowfall events during IOP SNEX 2014. The accumulated LWE is measured with a Pluvio^2 200 instrument, temperature and relative humidity are measured with at an ARM surface meteorological station at the height of 10 m, and wind speed is measured with a Gill anemometer at the height of 1.2 m next to the PIP.

		Temperature (°C)		RH (%)		Wind (m s^{-1})	
Date (UTC)	LWE (mm)	Min	Max	Min	Max	Mean	Max
2100 31 Jan–0600 1 Feb	7.4	−9.8	−8.9	84	91	1.6	2.9
1000–1600 1 Feb	1.4	−7.9	−7.0	90	93	1.4	2.3
1600–1900 2 Feb	1.7	−5.4	−5.2	90	94	1.1	1.7
0400–0900 12 Feb	0.8	−1	0	96	98	0.6	2.0
2100 15 Feb–0200 16 Feb	2.6	−2.1	−1	86	97	1.9	2.7
1600 21 Feb–0330 22 Feb	5.0	−2.7	0	88	98	2.1	3.4
0500–0700 15 Mar	0.3	−2.0	−1.3	93	95	0.7	2.3
0800–1900 18 Mar	4.4	−3.8	−1.8	76	96	1.2	2.7
0000–2000 19 Mar	1.5	−7.3	−3.7	76	95	1.2	3.3
1600–2350 20 Mar	6.1	−4.3	−1.3	89	97	2.0	3.4

section 3b. The factor for each event is determined by matching precipitation accumulation measured by the Pluvio^2 200 gauge and calculated from PIP observations. The diameter correction factor, and therefore the retrieved $m(D)$, are adjusted until the two accumulations match. The factor values vary from 0.7 to 0.9. The commonly used correction value in the majority of the studied cases is 0.82. This value is close to the mean value of 0.85, which is derived for the ratio between maximum side dimension and maximum horizontal dimension in Szyrmer and Zawadzki (2010) for small-sized particles. In contrast, Schmitt and Heymsfield (2010) obtained 0.77 as an averaged value of scaling factor between the diameter of the 2D projection and the maximum dimension of a 3D fractal snowflake.

Note that, as was discussed before, the used correction factor is not necessarily describing only the differences between the observed and true diameter but also addresses the limitations for observing the area ratio. It was noticed that there is a correlation between the corresponding correction factor and cloud-top height. With higher cloud, the applied correction was smaller. The particle shape seems to be the dominant contributor to the factor, but truncation of PSD has an influence as well. As was estimated in section 3c, the left side of the truncation with small $D_{\mathrm{deq},0}$ can result in underestimation of precipitation rate and thus, in the comparison with gauge measurements, is compensated for by assuming a higher correction factor.

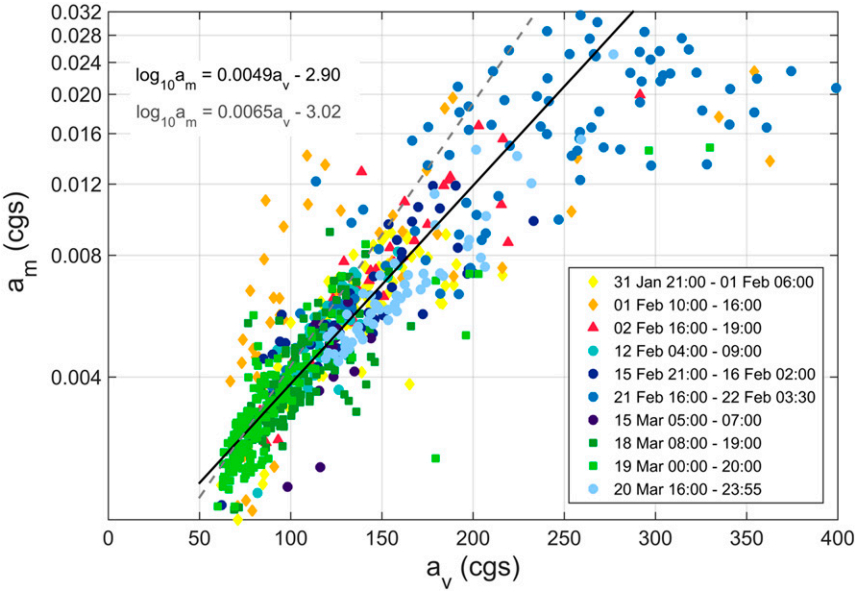


FIG. 4. Prefactors of the $m(D)$ relation as a function of prefactors of the $v(D)$ relation specified for each studied snow case in cgs units. The black solid line is the fit for the studied dataset, and the dashed gray line is the fit from the Szyrmer and Zawadzki (2010) study for comparison.

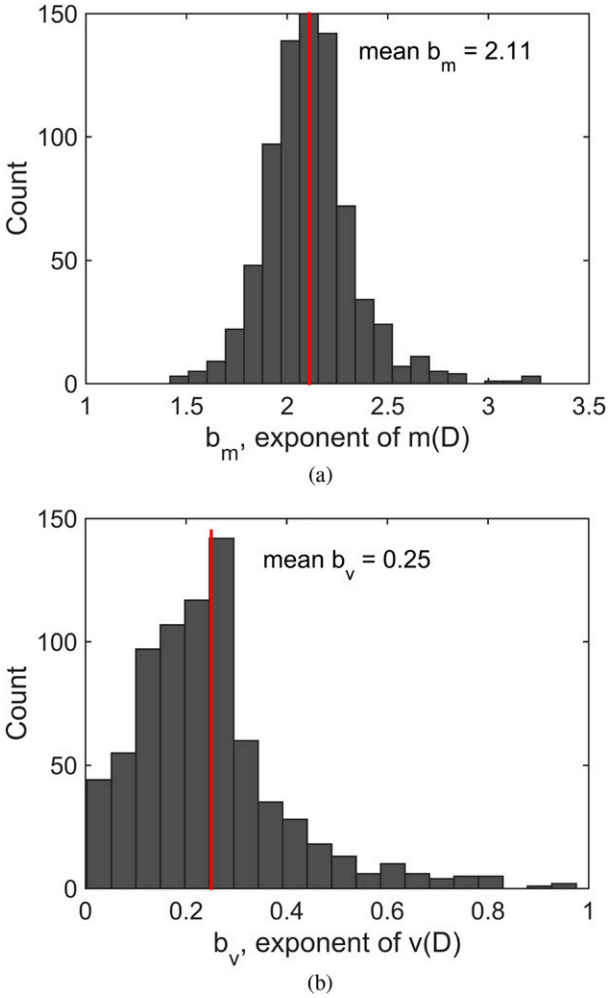


FIG. 5. Histograms of exponents of the (top) $m(D)$ and (bottom) $v(D)$ relations.

b. *The time series of $m(D)$ and $v(D)$ relations*

The prefactor values a_m and a_v of 5 min for all studied case are shown in Fig. 4. The cgs units are used. The fit to the dataset is performed by applying the total least squares method (Petras and Bednarova 2010). For comparison, the Szyrmer and Zawadzki (2010) relation is also plotted in Fig. 4. Their fit is based on nine events, assuming the exponent values to be constants, that is, $b_m = 2$ and $b_v = 0.18$. For low values of a_m and a_v, which represent low-density aggregates, the retrieved values of this study are aligned well with the Szyrmer and Zawadzki (2010) relation. The difference starts to appear as a_v increases, indicating the presence of denser, possibly more rimed, particles. This is expected because the Szyrmer and Zawadzki (2010) study is mainly based on observations of low-density aggregates. As was shown in earlier studies (e.g., Barthazy and Schefold 2006; Garrett and Yuter 2014), although the effect of riming on a snowflake fall speed is dependent on the crystal-type composition, riming generally both increases the value of prefactor a_v and modifies the shape of the dependence described by the exponent b_v. The cases with higher values of a_m and a_v (21–22 February and 20 March) have mean LWP values close to 250 g m^{-2}, and in general during the BAECC campaign the dual-channel microwave radiometer detected the presence of liquid water more than 80% of the time in snowfall (Petäjä et al. 2016); hence it is expected that the derived prefactor values in this study are higher. The histograms of exponent values of $m(D)$ and $v(D)$ relations for all of the cases are shown in Fig. 5. The mean exponent value of the $m(D)$ relation is 2.11, which is higher than the mean value of 1.9 found by Szyrmer and Zawadzki (2010). In other published studies, the exponent has varied from 1.4 for aggregates of unrimed radiating assemblages of dendrites to 3.0 for lump graupel (Locatelli and Hobbs 1974), and from 1.8 for needles and columns to 2.3 for side planes (Mitchell et al. 1990). In a theoretical study (Schmitt and Heymsfield 2010) of fractal properties of aggregates, the exponent was found to vary between 2.0 and 2.3. The exponent of the $v(D)$ relation has a mean value of 0.25. As a comparison, the literature values vary from 0.12 for aggregates of unrimed side planes to 0.66 for lump graupel (Locatelli and Hobbs 1974; Barthazy and Schefold 2006).

TABLE 2. The median prefactors and exponents of $m(D)$ and $v(D)$ relations in three ranges of LWP (g m^{-2}).

	$0 < \cdots \leq 100$	$100 < \cdots \leq 320$	>320
a_m (g cm$^{-b_m}$)	0.0046	0.0053	0.022
b_m	2.1	2.1	2.3
a_v (cm$^{1-b_v}$ s^{-1})	69	72	110
b_v	0.20	0.24	0.33

The median values of the prefactors and exponents of the $m(D)$ and $v(D)$ relations are computed in three different regions of LWP to illustrate the changes in values between different particle properties (Table 2). The increased LWP is considered to be an indicator of riming; hence the first region represents unrimed particles, the second represents rimed particles, and the third represents graupel or heavily rimed type. The time series are computed for an ensemble of particles that fell during 5-min time intervals; hence the factor values are not only describing the riming processes of a single particle but also possibly changes in the crystal-type composition. The change from unrimed to rimed particles can be seen as the increase in a_m. This value increases by ~20% if values of unrimed and rimed particles are compared and by a factor of 5 when unrimed particles are compared with the graupel. Erfani and Mitchell (2017) have estimated the ratio between the prefactors for unrimed and rimed particles to be 2.12, which falls within the range of our observations.

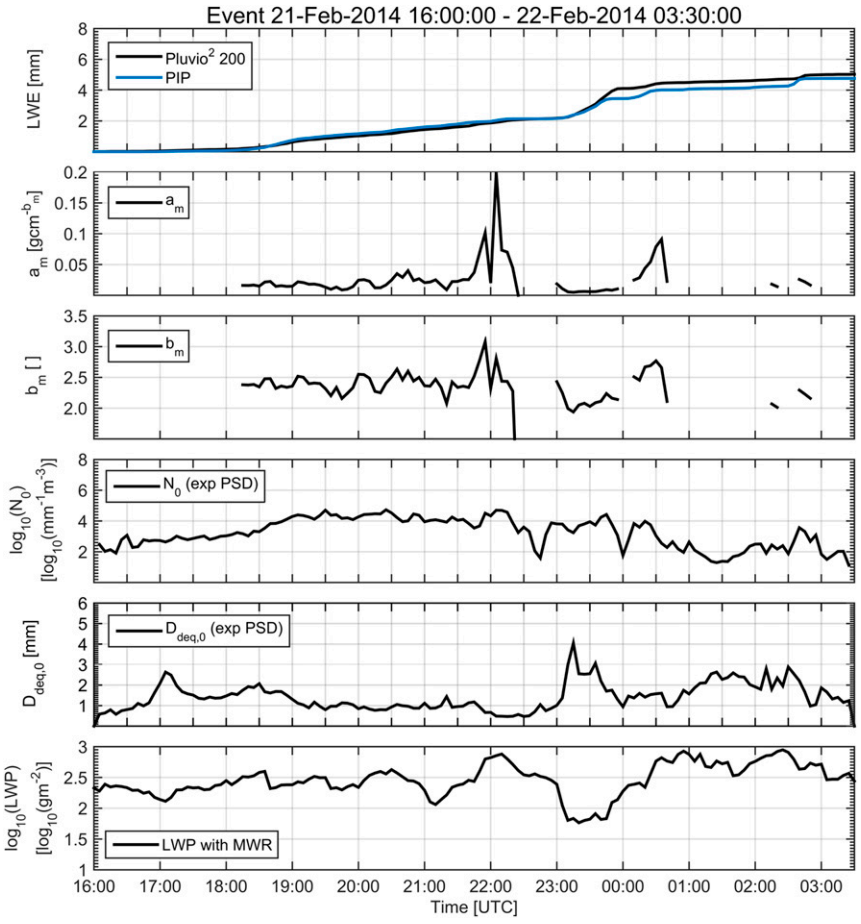


FIG. 6. Summary time series of the event on 21–22 Feb: (top) accumulated LWE derived from the mass estimate and velocity fit of PIP (colored solid line) and measured with a Pluvio^2 gauge (black solid line), factors (second from top) a_m and (third from top) b_m of the $m(D)$ relation, (third from bottom) intercept parameter N_0 of exponential mean PSD of 5 min, (second from bottom) median volume diameter of the exponential mean PSD of 5 min as a function of D_{deq}, and (bottom) LWP measured with a two-channel radiometer.

The computed median values of the exponent b_m are more or less the same for unrimed and rimed particles but increase noticeably for graupel. The earlier studies, for example, Locatelli and Hobbs (1974), show the exponent to be higher for rimed particles. Based on the conceptional study of Heymsfield (1982), at the early stages of riming, the diameter size is not increasing as the water droplets accrete to the spaces between crystal branches. As the particle reaches the graupel stage, riming also increases D. This assumption is applied, for example, in the parameterization of the cloud microphysics scheme by Morrison and Milbrandt (2015). Erfani and Mitchell (2017) showed that, on the basis of their dataset, the exponent values are similar for unrimed and rimed particles, which is in line with the results of our study.

1) EVENT ON 21–22 FEBRUARY: RAPID TRANSITION FROM RIMING TO AGGREGATION

To illustrate the findings of this study, two different cases are selected to show the changes in $m(D)$. The summary image of the event that took place on 21–22 February is shown in Fig. 6. This snow event is an example of a case in which both riming and aggregation processes are present. The strongest accumulation is occurring between 2300 and 0000 UTC, when large aggregates are observed (Kneifel et al. 2015). This can be seen in Fig. 6 as a_m, b_m, and LWP decrease while median volume diameter $D_{\mathrm{deq},0}$ increases. During this time period the exponent b_m ranged between 1.9 and 2.16; during the rest of the event it is closer to 2.5, with maximum values occurring at 2200 UTC coinciding with the peak in LWP. In the previous section it was

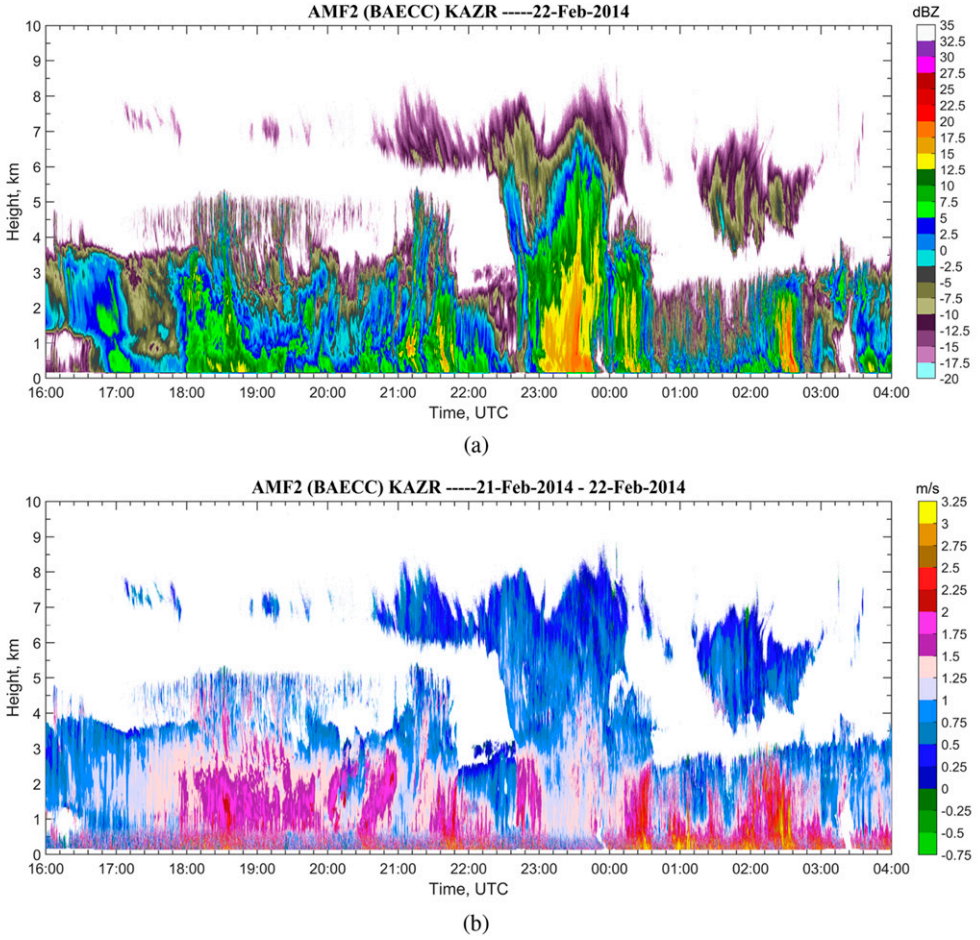


FIG. 7. (a) Reflectivity factor and (b) reflectivity-weighted fall velocity of AMF2 Ka-band ARM zenith radar (KAZR) on 21–22 Feb.

discussed that the exponent b_m is independent of riming and only starts to increase at the graupel stage of particle growth. The increased values of b_m during this event indicate graupel formation, and small graupel-like particles are observed in the PIP videos, example images of which can be found in (Kneifel et al. 2015). The mean a_m for the whole event is approximately $0.025\,\mathrm{g\,cm^{-b_m}}$, although during the aggregation time period it drops to an average of $0.006\,\mathrm{g\,cm^{-b_m}}$. The same features can be seen in the vertically profiling Ka-band radar observations in Fig. 7. An increase in reflectivity-weighted fall velocities indicates the possibility of riming. The highest precipitation intensity took place during the aggregation time period. This can be seen as increased values of reflectivity factor between 2300 UTC 21 February and 0000 UTC 22 February.

2) EVENT ON 18 MARCH: AGGREGATION

The summary image of this case is shown in Fig. 8. This event has two precipitation periods, one at 0500–1200 UTC and the other at 1400–1900 UTC; between those periods snowfall ceased almost completely. The snow particle type seems to be fairly constant during both time periods, which is why this case is classified as one event. The overall level of the prefactor a_m is $0.0042\,\mathrm{g\,cm^{-b_m}}$; during the morning period the mean exponent of $m(D)$ is 2.04, and in the afternoon it is 2.12. Also the values of $D_{\mathrm{deq},0}$ are relatively high, reaching a maximum of 5.8 mm, which indicates the presence of large aggregates. The values of LWP are actually very high during the morning precipitation period, indicating possible riming. Because the particle sizes are large during that time, the relative increase of the mass due to collection of supercooled water droplets on ice particles is small. Hence an increase in the prefactors of the $v(D)$ and $m(D)$ relations as a result of riming is not observed.

c. *Event-average Z_e–S relations*

The equivalent reflectivity factor Z_e [Eq. (10)] and the precipitation rate S [Eq. (8)] are calculated every

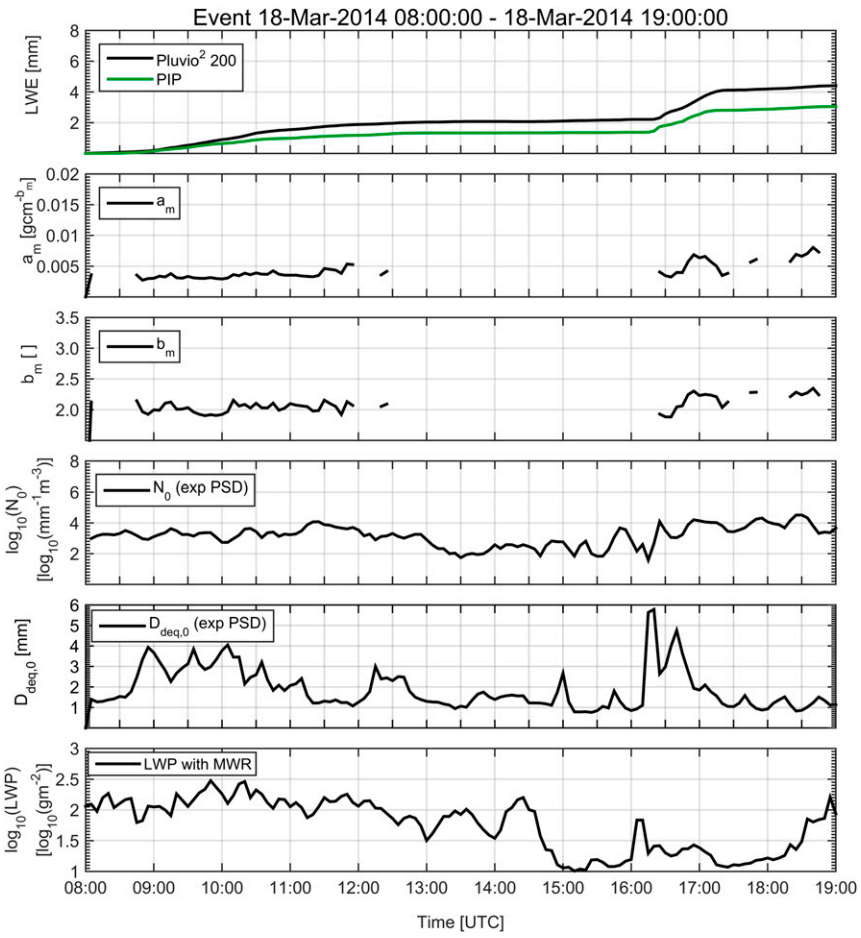


FIG. 8. As in Fig. 6, but for 18 Mar.

5 min for all studied events. The prefactor a_{zs} and exponent b_{zs} of Z_e–S are computed by applying the total least squares method (Petras and Bednarova 2010) and are given in Table 3. The total least squares method is applied because it considers errors in both variables Z_e and S (Lee and Zawadzki 2005). For the two example events described above, the scatterplot of Z_e versus S and the derived power-law fits are shown in Fig. 9. The derived Z_e–S relations are checked by applying them to PPI scans from the Ikaalinen C-band weather radar, and the estimated accumulated LWE is compared with the measurements by the FMI operational gauges. Accumulation maps are shown in Fig. 10. The vertical trends can be significant in snowfall, as can be observed, for example, in Fig. 7, and changes in reflectivity factor aloft can result in a discrepancy in the observed S and a bias in the calculated accumulation on the ground. The PPI scan of lowest elevation angle is used to measure as close to the ground as possible, but nevertheless the uncertainty of the estimated S increases with the distance from the radar.

On 21–22 February the precipitation rate and particle type are varying. The highest accumulation occurs between 2300 and 0000 UTC. During this time period, the prevailing observed particle type (aggregates) differs from the otherwise observed ones throughout the snow event. Because of this behavior,

TABLE 3. The prefactors and exponents of the $Z_e = a_{zs}S^{b_{zs}}$ relation during BAECC SNEX 2014, with Z_e in millimeters to the sixth power per meter cubed and S in millimeters per hour.

Date (UTC)	a_{zs}	b_{zs}
2100 31 Jan–0600 1 Feb	52.5	1.29
1000–1600 1 Feb	143.4	1.41
1600–1900 2 Feb	102.3	1.19
0400–0900 12 Feb	160.0	1.65
2100 15 Feb–0200 16 Feb	114.3	1.32
1600 21 Feb–0330 22 Feb	146.5	1.30
0500–0700 15 Mar	143.2	1.44
0800–1900 18 Mar	290.9	1.41
0000–2000 19 Mar	781.8	1.52
1600–2350 20 Mar	87.3	1.61

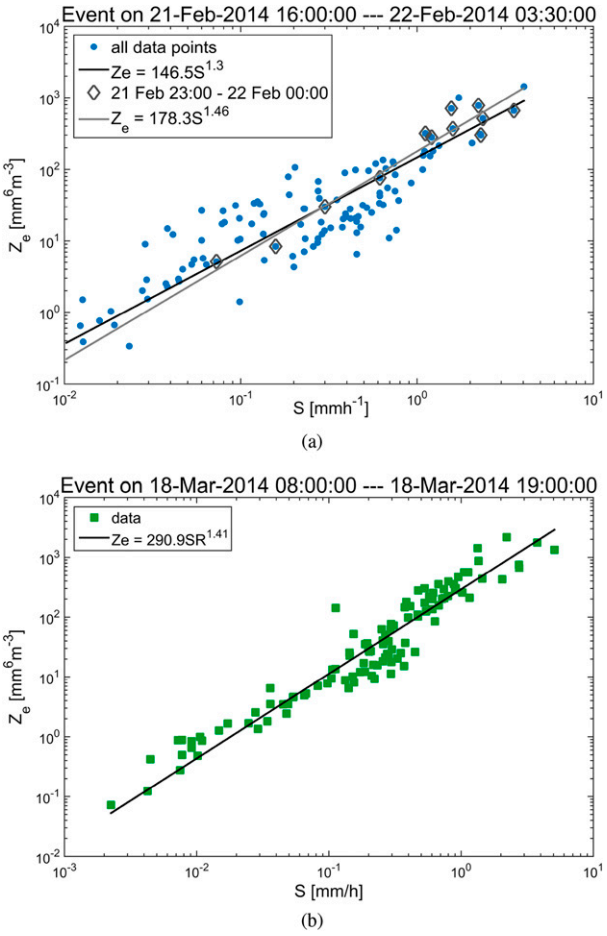


FIG. 9. Scatterplots of Z_e vs S with the power-law fit (solid black line) using the total least squares method on snow events of (a) 21–22 Feb and (b) 18 Mar. In (a), another fit (gray solid line) is performed that takes into account only observations during the highest accumulation (data points marked with gray diamonds).

the average Z_e–S relation for the whole event overestimates the accumulation. The accumulation is accurately estimated over Hyytiälä (the solid black dot in the east with value of 5.1 mm), however. On that day the weather front was approaching southern Finland from the southwest and the heavier precipitation covered the inspected region before it reached Hyytiälä at 2300. Hence the factors that were defined on the basis of the measurements and retrievals at the Hyytiälä site are not valid for the surrounding area. If compared with LWE accumulation estimated with FMI operational factors, the overestimation is even bigger, except in the region of the strongest accumulation. To study this result, another Z_e–S fit is performed for this event, taking only the data points that correspond to the highest accumulation (shown in Fig. 9). The resulting accumulation map is given in Fig. 11. As expected, this estimate gives a better result.

On 18 March the derived factors estimate well the accumulated LWE, because the variability both in snow type as well as in precipitation intensity is smaller. The FMI operational factors clearly overestimate the accumulation for this event.

To compare the performance of the radar-estimated precipitation accumulation with gauge measurements for all of the events, a density scatterplot of the hourly accumulations is presented in Fig. 12. A comparison of the total event accumulation is shown in Fig. 13. The root-mean-square error (RMSE) and coefficient of determination r^2 are defined for both analyses. For comparison, the results of applying the FMI operational factors are also plotted. For the hourly accumulations in Fig. 12, use of the case-specific BAECC SNEX factors yields the stronger correlation, with a notably higher value of r^2; nevertheless, the RMSE is smaller when utilizing the FMI operational relation. There is actually an overestimation of the hourly accumulations when applying the SNEX relations, especially for the events with higher precipitation rate. The results of total LWE accumulations for each event that are given in Fig. 13 show similar trends. The case-specific SNEX relations perform better than the FMI relation both in terms of correlation and RMSE. The discrepancy between the radar-estimated accumulation and gauge measurements, both with the hourly and the eventwise total precipitation, largely originates from the snow events of 31 January–1 February and 21–22 February, both of which are the cases with large variations in $m(D)$ and Z_e–S relations.

While performing the intercomparison with gauges, the measurement errors of the gauges must also be considered; for example, they are known to undercatch snowfall because of the wind (Rasmussen et al. 2012). These errors might explain the bias of the radar-based estimates. In a similar way, in Huang et al. (2015) the bias of the radar-based daily accumulation against gauge measurements was close to 30%, when eventwise Z_e–S relations obtained from 2DVD data were applied.

A general Z_e–S relation is defined including all of the 5-min values from all studied snowfall events (Fig. 14). The large variability of values for the fit is noticeable. For the prefactor a_{zs}, the error limits with percentiles of 5% and 95% are determined while constraining exponent b_{zs} to a constant value of 1.23.

d. *Instantaneous Z_e–S relations and their dependence on PSD and microphysical parameters*

As discussed in the previous section, changes in microphysical snow growth processes during a snowstorm

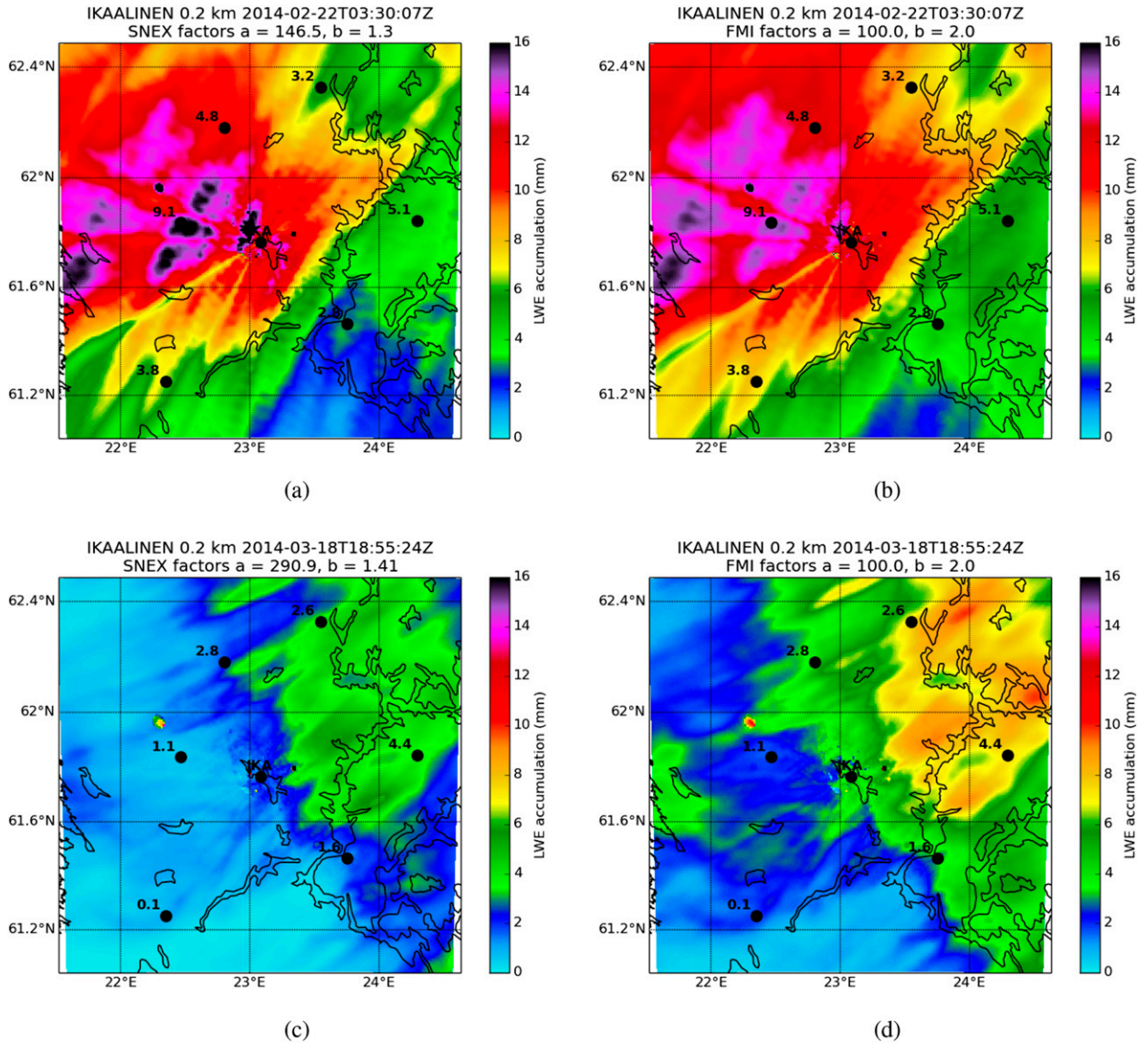


FIG. 10. The accumulation maps of the defined Z_e–S factors applied with Ikaalinen radar scans in comparison with the operational FMI factors for snow events on (a),(b) 21–22 Feb and (c),(d) 18 Mar for (left) case-specified factors and (right) FMI operational factors. Solid black dots are locations of the automatic FMI gauges, and the numbers indicate the accumulated LWE measured with the gauges (mm). The color bar shows the values of the estimated accumulated LWE with the radar.

result in variability in coefficients of Z_e–S relation. There is also a large variance in Z_e–S between the storms, as shown in Table 3, and for reference some of the factor values presented in the literature are given in Table 4. Note that the prefactor of the relation is very different depending on whether it is described as a function of a melted diameter or as an equivalent spherical ice particle diameter (as in this study); the conversion from (Smith 1984) is presented and used in Table 4. In the past decades, several studies have been dedicated to this topic, and it has been stated that the values of a_{zs} and b_{zs} depend on different parameters, such as the crystal type, degree of riming and aggregation, density, and terminal velocity (Rasmussen et al. 2003). In their theoretical analysis, Rasmussen et al. (2003) showed the dependence of the prefactor a_{zs} to particle size distribution through the intercept parameter N_0, and they have derived two relations for dry and wet/dense snow. In their study, the exponent b_{zs} is the same for both relations and the difference in prefactor is determined by the different density–size relations.

Here we present a similar theoretical analysis to study in more detail the parameters that influence the Z_e–S

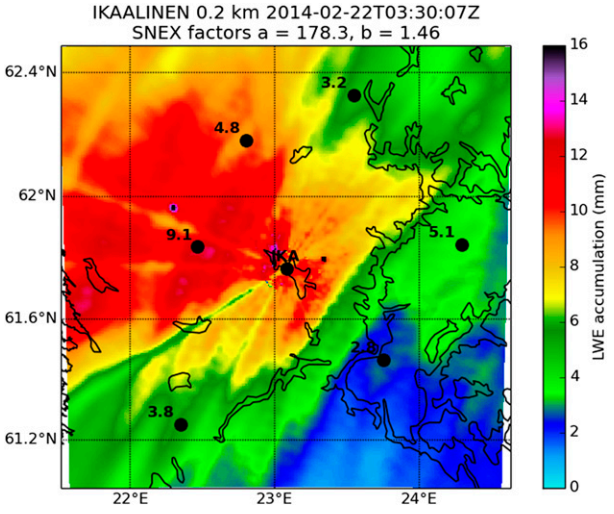


FIG. 11. The accumulation map utilizing the fitted Z_e–S factors for the time period of the maximum precipitation rate over Hyytiälä applied with Ikaalinen radar scans on 21–22 Feb.

relation. The derived relations can be treated as instantaneous relations because during precipitation events the input parameters change. This is also the reason why the derived relations here differ from the ones presented in Tables 3 and 4. Assuming gamma PSD in the form of $N(D) = N_0 D^{\mu} \exp(-\Lambda D)$ and rewriting the equivalent reflectivity factor in Eq. (10), Z_e becomes

$$\begin{aligned} Z_e &= \frac{36}{\pi^2 \rho_{\text{ice}}^2} \frac{|K_{\text{ice}}|^2}{|K_w|^2} \int_0^{\infty} (a_m D^{b_m})^2 N_0 D^{\mu} \exp(-\Lambda D)\, dD \\ &= \frac{36}{\pi^2 \rho_{\text{ice}}^2} \frac{|K_{\text{ice}}|^2}{|K_w|^2} a_m^2 N_0 \Lambda^{-(2b_m+\mu+1)} \Gamma(2b_m + \mu + 1) \\ &= F_{Z_e} \Lambda^{-(2b_m+\mu+1)}, \end{aligned} \tag{12}$$

and the precipitation rate Eq. (8) can be expressed as

$$\begin{aligned} S &= \frac{1}{\rho_w} \int_0^{\infty} a_m D^{b_m} a_v D^{b_v} N_0 D^{\mu} \exp(-\Lambda D)\, dD \\ &= \frac{1}{\rho_w} a_m a_v N_0 \Lambda^{-(b_m+b_v+\mu+1)} \Gamma(b_m + b_v + \mu + 1) \\ &= F_S \Lambda^{-(b_m+b_v+\mu+1)}. \end{aligned} \tag{13}$$

The difference from Eqs. (8) and (10) is that the integrals are infinite for obtaining the analytical solution of the gamma function. Here a dependence of the Z_e–S relation on different parameters is studied and the impact of the truncation is not considered. By combining Eqs. (12) and (13), the relation between Z_e and S can be given as

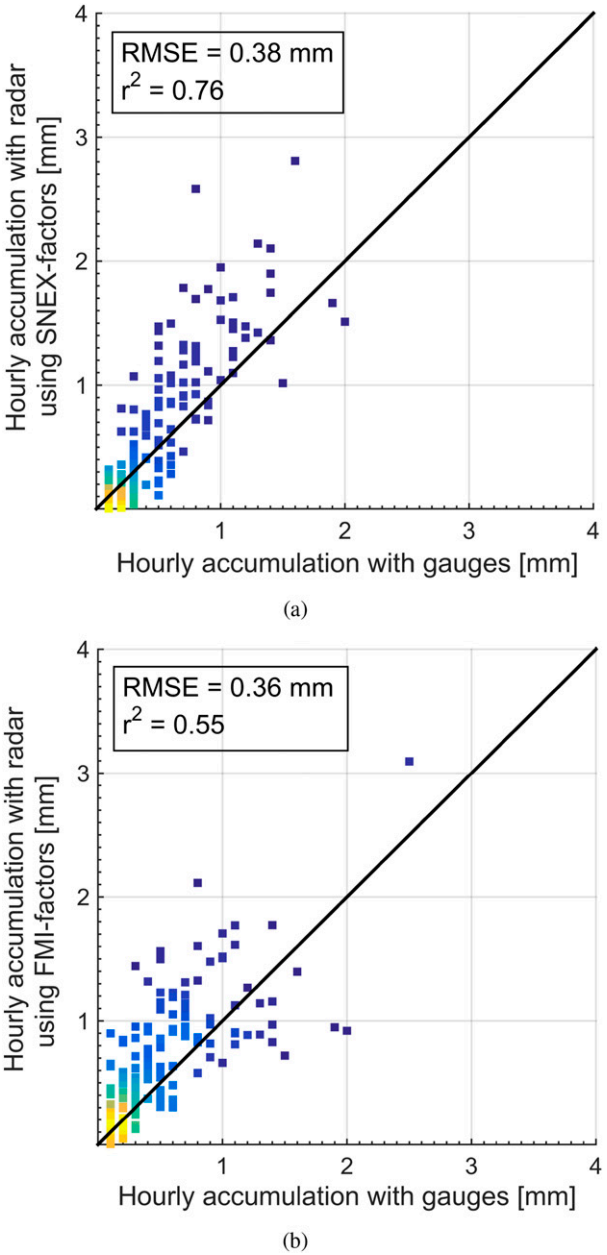


FIG. 12. The scatterplot of the hourly accumulation measured by the operational gauges of FMI with respect to estimated accumulation from the Ikaalinen radar PPI scans with Z_e–S relation of (a) case-specific SNEX factors shown in Table 3 and (b) FMI operational factors $a_{zs} = 100.0$ and $b_{zs} = 2.0$.

$$\begin{aligned} Z_e &= F_{Z_e} F_S^{[-(2b_m+\mu+1/b_m+b_v+\mu+1)]} S^{2b_m+\mu+1/b_m+b_v+\mu+1} \\ &= a_{zs} S^{b_{zs}}. \end{aligned} \tag{14}$$

As can be seen, the exponent of Z_e–S depends on the exponent terms of the $m(D)$ and $v(D)$ relations and PSD shape parameter μ. Assuming that the PSD follows the exponential functional form ($\mu = 0$) and choosing a

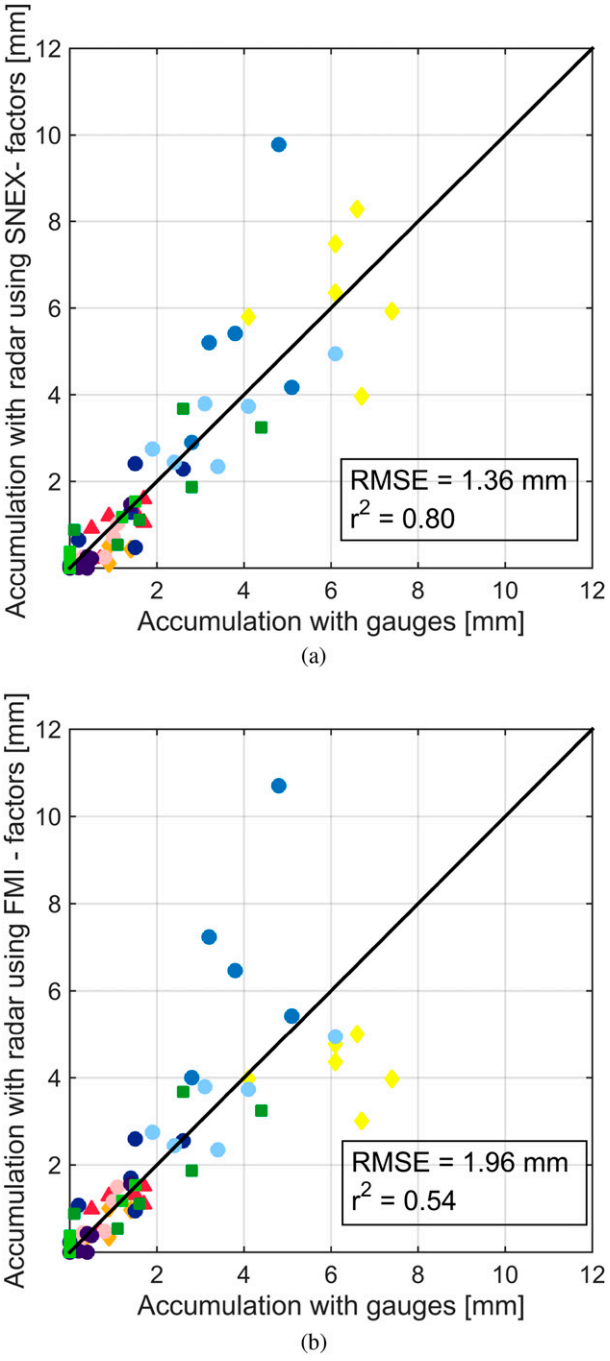


FIG. 13. The scatterplot of the event accumulation (events are shown with the symbols that were defined in Fig. 4) measured by the operational gauges of FMI with respect to estimated accumulation from the Ikaalinen radar PPI scans with Z_e–S relation of (a) case-specific SNEX factors and (b) FMI operational factors.

typical value for aggregates $b_m = 2$ and constant velocity ($b_v = 0$), the value of $b_{zs} = 5/3$ is derived. This is the value reported by Rasmussen et al. (2003). For an exponential PSD, the b_{zs} values seem to be around 1.5–1.7, depending on values of b_m and b_v. Using the mean values of the BAECC SNEX cases ($b_m = 2.11$ and $b_v = 0.25$), the value of $b_{zs} = 1.55$ is found. It is also close to the value of 1.59 presented by Bukovcic et al. (2015). Tiira et al. (2016) presented a normalized histogram of values of μ during snow cases for the winter of 2014/15 in Hyytiälä. It was found that μ ranged from −0.9 to 3. Using these values, the b_{zs} values are found to vary between 1.76 and 1.29.

The dependence of prefactor a_{zs} on microphysical parameters is more complex; it is a function of all parameters of $m(D)$, $v(D)$, and $N(D)$ relations [Eq. (14)]. Using the mean values found from BAECC 2014 cases, the a_{zs} is proportional to $N_0^{-0.55}$. This dependence of a_{zs} on N_0 is similar to the ones found in Rasmussen et al. (2003) and Bukovcic et al. (2015).

In this study the N_0 dependence is also investigated experimentally and is depicted in Fig. 15. The exponent b_{zs} is computed for every 5 min with Eq. (14), assuming $\mu = 0$. Huang et al. (2015) showed that the different factors of Z_e–S have dependence on LWP. The LWP is a proxy for riming and therefore is related to the changes in a_m and a_v, and thereby also in a_{zs}. The relation between a_{zs}, N_0, and LWP is shown in Fig. 15. The studied cases are divided into groups on the basis of the selected $D_{\mathrm{max,obs}} - D_{\mathrm{max,true}}$ correction factor, which is related to the prevailing particle shape. For each group, the fits for a_{zs} as a function of $\log_{10}(N_0)$ are performed separately with the total least squared method (Petras and Bednarova 2010). The computed exponent values of N_0 vary between −0.64 and −0.50. The dependence of a_{zs} on N_0 is strong, especially during periods with low precipitation rate. This result explains, for example, the a_{zs} value of 781.8 found for the 19 March event, because the accumulation during the whole event (0000–2000 UTC) was only close to 1.5 mm.

The prefactor a_{zs} also depends on riming. For example, for the snow events on 18 and 19 March, there was very little riming during the event and particle type was categorized as low-density aggregates. The N_0 exponent is −0.64 (Fig. 15). In contrast, the lighter-blue solid line, which corresponds to the 21–22 February event, is noticeably lower than the other lines. The N_0 exponent is −0.50. This is the event during BAECC SNEX with the highest LWP values and in which for most of the time the particles were moderately or heavily rimed.

To separate the effects of riming and change in N_0, a partial correlation analysis was carried out. The partial correlations of log values of a_{zs}, LWP, and N_0 were computed. It was found that the partial correlation between $\log_{10}(a_{zs})$ and $\log_{10}(N_0)$, while controlling for $\log_{10}$(LWP), is −0.97 and that between $\log_{10}(a_{zs})$ and $\log_{10}$(LWP), while controlling for $\log_{10}(N_0)$, is −0.46.

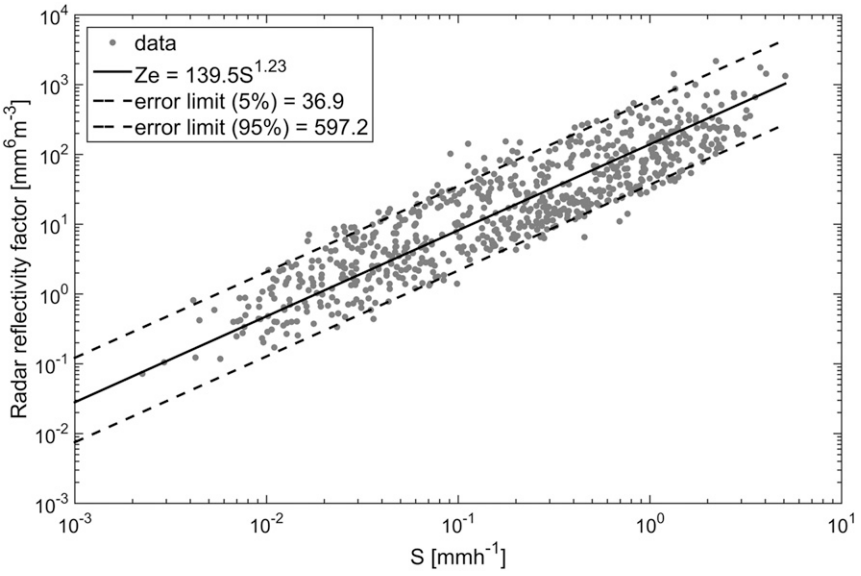


FIG. 14. The average fit for all studied BAECC 2014 cases, with error limits defined at percentiles of 5% and 95% and constraining exponent b_{zs} to the value 1.23.

This analysis indicates that the prefactor of Z_e–S depends more on N_0 than on $\log_{10}$(LWP) or degree of riming.

The dependence of the prefactor a_{zs} on LWP estimated as $a_{zs}/N_0^{b_{N_0}}$ and presented as a function of the measured mean LWP is shown in Fig. 16. The exponent b_{N_0} can be written as $b_{N_0} = 1 - (2b_m + 1)/(b_m + b_v + 1)$ assuming the exponential PSD. The resulting scatterplot shows that a_{zs} and LWP are related, but the relation is not very strong. The LWP data are noisy, but the fitted exponent describing the dependence of the prefactor a_{zs} on LWP is −0.21. Assuming that b_{N_0} is −0.55, with the average value of all SNEX cases, the relation shown in Fig. 16 seems to estimate a_{zs} well; the correlation coefficient is 0.93 as presented in Fig. 17.

5. Conclusions

The connection between microphysical properties of snow and radar observations is demonstrated by studying the snowfall events recorded during the BAECC campaign that took place in southern Finland. The key instruments employed in this study are the video disdrometer, Particle Imaging Package, and weighing precipitation gauge. These instruments are used to retrieve time series of microphysical parameters of falling snow. The snowflake $m(D)$ relations are estimated on temporal scales of several minutes by applying the hydrodynamic theory to PIP observations of particle size and fall velocity. Because PIP observes falling hydrometeors from a side, the errors associated with the observation geometry and the measured particle size distribution are addressed by devising a simple correction procedure. The correction factor is applied to the diameter, when calculating the Reynolds number. A single factor is chosen for each snow event by comparing the estimated accumulated precipitation with gauge measurements. Note that the selected factor is not necessarily describing only the discrepancy between true and observed diameter but can also correspond to the limitations of modeling the irregular particle as an ellipsoid, the effect of the restricted single projection view of the particle, and truncation of the observed particle size distribution.

In this study, it is shown how changes in the retrieved $m(D)$ relation correspond to transitions from one snow growth process to another—for example, between aggregation and riming. Furthermore, these can be linked to radar and microwave radiometer observations. It is

TABLE 4. The prefactors and exponents of the $Z_e = a_{zs}S^{b_{zs}}$ relation in the literature. Studies that are marked with an asterisk are converted with $Z_e = 0.224Z$ (Smith 1984).

Literature	a_{zs}	b_{zs}
Gunn and Marshall (1958)*	448	2
Sekhon and Srivastava (1970)*	399	2.21
Ohtake and Hemni (1970)*	90–739	1.5–1.9
Puhakka (1975)*	235	2
Saltikoff et al. (2010)	100	2
Huang et al. (2010)	106–305	1.11–1.92
Szyrmer and Zawadzki (2010)	494	1.44
Huang et al. (2015)	130–209	1.44–1.81

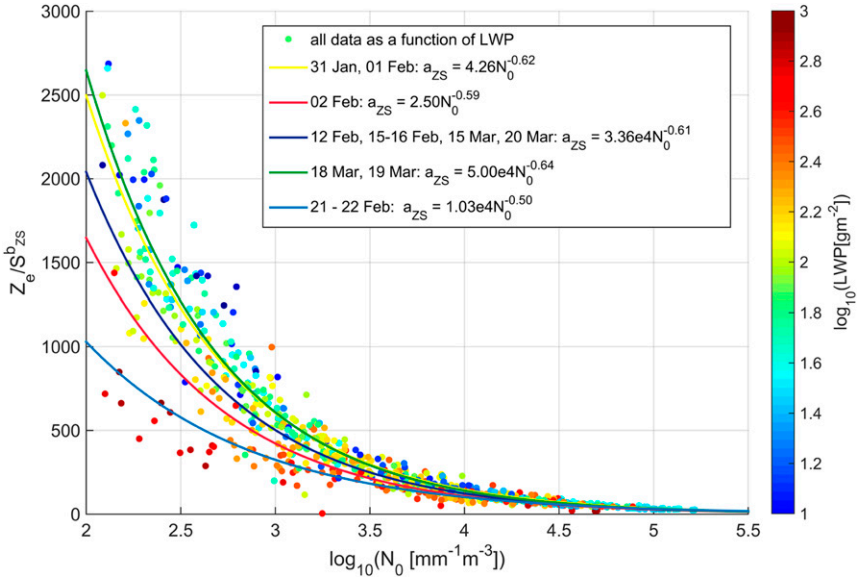


FIG. 15. The prefactor of Z_e–S as a function of the intercept parameter N_0 and LWP measured with the radiometer. The data points are colored according to the 5-min mean LWP measured with the radiometer. The fits of $a_{zs}(N_0)$ are shown separately for grouped cases. The dark-blue line is the cases with a chosen correction factor of 0.82,the light-blue line is the 21–22 Feb case with a correction factor of 0.82 and also observations of graupel, the yellow line is for 31 Jan–1 Feb, with a correction-factor value of 0.70 and a mean $D_{\mathrm{deq},0}$ that is close to 1.0 mm, the green line is for 18–19 Mar, with a correction-factor value of 0.70 and a mean $D_{\mathrm{deq},0}$ that is close to 2.0 mm, and the red line is for 2 Feb, with a correction factor of 0.9.

observed that the prefactor of the $m(D)$ relation is a dominating parameter to describe the changes in these processes. With the observed PSDs, fitted $v(D)$ relations, and retrieved $m(D)$ relations the time series of the equivalent reflectivity factor Z_e and precipitation rate S are computed. For each studied event, a single Z_e–S relation is derived. The case-specific relations are used to compare the radar-based snowfall estimates with gauge observations. This comparison acts also as an indirect confirmation of the validity of the $m(D)$ retrievals. It is shown that the prefactor a_{zs} is the main factor that affects the radar-based snowfall estimation.

In addition to the case-specific Z_e–S, instantaneous Z_e–S relations are computed using retrieved PSD and $m(D)$ parameters on temporal scales of few minutes. It was shown that during a snowstorm the parameters of the instantaneous Z_e–S can vary, and these are typically different from the case-specific Z_e–S ones. This can be clearly seen while comparing the exponents of the Z_e–S. From the analysis of the instantaneous relations it was found that the exponent of Z_e–S mainly depends on the exponent of the $m(D)$. Note that ranges over which the exponents of instantaneous and case-specific relations vary are different. The event-specific exponent of Z_e–S varies between 1.19 and 1.61 in studied events and can be as high as 2 as reported in the literature, whereas for the instantaneous relations the exponent varies between 1.5 and 1.7. It is foreseen that the instantaneous relations will be used to estimate uncertainties of quantitative precipitation estimates.

The prefactor of Z_e–S, a_{zs}, mainly depends on the intercept parameter N_0 of PSD and prefactors of the $m(D)$ and $v(D)$ relations. The changes in the prefactors a_m and a_v can be attributed to changes in microphysical processes, such as riming. To study this, observations of liquid water path were used as a proxy for degree of riming. The a_{zs} values are shown to be connected to

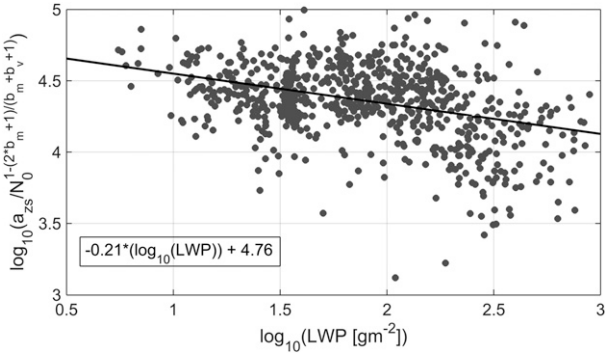


FIG. 16. The dependence of prefactor $a_{zs}/N_0^{b_{N_0}}$ as function of LWP in log scale.

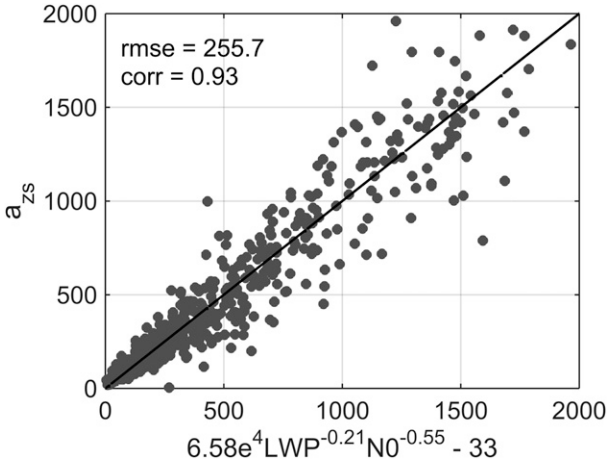


FIG. 17. Scatterplot of derived 5-min time series of a_{zs} assuming theoretical b_{zs} with exponential PSD vs parameterized a_{zs} with dependence of $N_0^{-0.55}$ defined by the mean values of BAECC SNEX cases and the dependence of LWP −0.21 from the linear regression. The RMSE has the units of a_{zs} ($\mathrm{mm}^{b_{zs}-6}\,\mathrm{m}^{-3}\,\mathrm{h}^{-1}$).

LWP. The relative importance of LWP and N_0 to the prefactor a_{zs} is also investigated. It is shown that N_0 is the main contributor to the changes in a_{zs}. The role of riming is smaller but still noticeable. A parameterization expressing a_{zs} as a function N_0 and LWP was also derived.

It is shown that quantitative precipitation estimation can be improved by using adjustable Z_e–S relations. In Rasmussen et al. (2003) an algorithm for adaptive Z_e–S is demonstrated in which the exponent b_{zs} was changing between fixed values for rain and snow and the prefactor a_{zs} was adjusted with gauge comparison.

Because of the strong dependence of the prefactor a_{zs} on N_0, the adaption should be based on N_0 or parameters related to the particle size distribution. With current routinely recorded meteorological data or with single-frequency radar measurements, there unfortunately is no established procedure to retrieve these parameters. An operational network of disdrometers (e.g., Parsivels) with the necessary spatial resolution could be utilized to scale the prefactor. With low precipitation intensity, also the prefactor of the $m(D)$ relation can explain partly the different values of the prefactor a_{zs}. In recent years, advances have been taken to retrieve the snow type from polarimetric radar measurements (e.g., Kennedy and Rutledge 2011; Bechini et al. 2013; Moisseev et al. 2015; Thompson et al. 2014; Grazioli et al. 2015). By identifying the snow type from the radar measurements, the prefactor could be changed accordingly. For single-polarization radar measurements, an averaged relation can be defined as was shown in Fig. 14, and the error limits can be utilized for probabilistic nowcasting of snowfall precipitation rate.

Acknowledgments. We acknowledge the contribution of the Hyytiälä station and University of Helsinki personnel for the daily tasks with measurements. Author AvL was funded by a grant of the Vilho, Yrjö and Kalle Väisälä Foundation and by SESAR Joint Undertaking Horizon 2020 Grant Agreement 699221 (PNOWWA). The research of author DM was supported by the Academy of Finland (Grant 305175) and the Academy of Finland Finnish Center of Excellence program (Grant 272041). Author WP acknowledges funding provided by Dr. Ramesh Kakar of the NASA Precipitation Measurement Missions Program and the GPM Mission. The instrumentation used in this study was supported by the NASA Global Precipitation Measurement Mission ground validation program and by the U.S. Department of Energy Office of Science ARM program.

REFERENCES

Abraham, F. F., 1970: Functional dependence of drag coefficient of a sphere on Reynolds number. *Phys. Fluids*, **13**, 2194–2195, doi:10.1063/1.1693218.

Atlas, D., M. Kerker, and W. Hitschfeld, 1953: Scattering and attenuation by non-spherical atmospheric particles. *J. Atmos. Terr. Phys.*, **3**, 108–119, doi:10.1016/0021-9169(53)90093-2.

Barthazy, E., and R. Schefold, 2006: Fall velocity of snowflakes of different riming degree and crystal types. *Atmos. Res.*, **82**, 391–398, doi:10.1016/j.atmosres.2005.12.009.

——, S. Göke, R. Schefold, and D. Högl, 2004: An optical array instrument for shape and fall velocity measurements of hydrometeors. *J. Atmos. Oceanic Technol.*, **21**, 1400–1416, doi:10.1175/1520-0426(2004)021<1400:AOAIFS>2.0.CO;2.

Battan, L., 1973: *Radar Observation of the Atmosphere.* The University of Chicago Press, 324 pp.

Bechini, R., L. Baldini, and V. Chandrasekar, 2013: Polarimetric radar observations in the ice region of precipitating clouds at C-band and X-band radar frequencies. *J. Appl. Meteor. Climatol.*, **52**, 1147–1169, doi:10.1175/JAMC-D-12-055.1.

Böhm, H., 1989: A general equation for the terminal fall speed of solid hydrometeors. *J. Atmos. Sci.*, **46**, 2419–2427, doi:10.1175/1520-0469(1989)046<2419:AGEFTT>2.0.CO;2.

Brandes, E., K. Ikeda, G. Zhang, M. Schönhuber, and R. Rasmussen, 2007: A statistical and physical description of hydrometeor distributions in Colorado snowstorms using a video disdrometer. *J. Appl. Meteor. Climatol.*, **46**, 634–650, doi:10.1175/JAM2489.1.

Bringi, V. N., and V. Chandrasekar, 2001: *Polarimetric Doppler Weather Radar: Principles and Applications.* Cambridge University Press, 636 pp.

Bukovcic, P., D. Zrnic, G. Zhang, and A. Ryzhkov, 2015: Snow variability in Oklahoma and Colorado characterized by 2D-video disdrometer and dual-polarization radar measurements. *37th Conf. on Radar Meteorology*, Norman, OK, Amer. Meteor. Soc., 3A.1. [Available online at https://ams.confex.com/ams/37RADAR/recordingredirect.cgi/id/31030.]

Cadeddu, M., 2014: Microwave radiometer (MWRLOS), ARM Mobile Facility TMP, University of Helsinki research station SMEAR II, Hyytiälä, Finland. Atmospheric Radiation Measurement (ARM) Climate Research Facility Data Archive, Oak Ridge, TN, accessed 17 March 2016, doi:10.5439/1046211.

Erfani, E., and D. L. Mitchell, 2017: Growth of ice particle mass and projected area during riming. *Atmos. Chem. Phys.*, **17**, 1241–1257, doi:10.5194/acp-2016-455.

FMI climateservice, 2014: Weather and climate in Finland. Finnish Meteorological Institute, accessed 16 September 2016. [Available online at http://ilmatieteenlaitos.fi/talvi-2013-2014.]

Fujiyoshi, Y., T. Endoh, T. Yamada, K. Tsuboki, Y. Tachibana, and G. Wakahama, 1990: Determination of a *Z–R* relationship for snowfall using a radar and high sensitivity snow gauges. *J. Appl. Meteor.*, **29**, 147–152, doi:10.1175/1520-0450(1990)029<0147:DOARFS>2.0.CO;2.

Garrett, T. J., and S. Yuter, 2014: Observed influence of riming, temperature, and turbulence on the fallspeed of solid precipitation. *Geophys. Res. Lett.*, **41**, 6515–6522, doi:10.1002/2014GL061016.

——, C. Fallgatter, K. Shkurko, and D. Howlett, 2012: Fall speed measurement and high-resolution multi-angle photography of hydrometeors in free fall. *Atmos. Meas. Tech.*, **5**, 2625–2633, doi:10.5194/amt-5-2625-2012.

——, S. E. Yuter, C. Fallgatter, K. Shkurko, S. Rhodes, and J. L. Endries, 2015: Orientations and aspect ratios of falling snow. *Geophys. Res. Lett.*, **42**, 4617–4622, doi:10.1002/2015GL064040.

Goodison, B., P. Louie, and D. Yang, 1998: WMO solid precipitation measurement intercomparison final report. World Meteorological Organization Tech. Doc. 872, IOM 67, 212 pp. [Available online at https://www.wmo.int/pages/prog/www/IMOP/publications/IOM-67-solid-precip/WMOtd872.pdf.]

Grazioli, J., D. Tuia, and A. Berne, 2015: Hydrometeor classification from polarimetric radar measurements: A clustering approach. *Atmos. Meas. Tech.*, **8**, 149–170, doi:10.5194/amt-8-149-2015.

Gunn, K., and J. Marshall, 1958: The distribution with size of aggregate snowflakes. *J. Meteor.*, **15**, 452–461, doi:10.1175/1520-0469(1958)015<0452:TDWSOA>2.0.CO;2.

Hanesch, M., 1999: Fall velocity and shape of snowflakes. Ph.D. thesis, Swiss Federal Institute of Technology, 123 pp., doi:10.3929/ethz-a-003837623.

Harrington, J., K. Sulia, and H. Morrison, 2013: A method for adaptive habit prediction in bulk microphysical models. Part II: Theoretical development. *J. Atmos. Sci.*, **70**, 349–364, doi:10.1175/JAS-D-12-040.1.

Heymsfield, A. J., 1982: A comparative study of the rates of development of potential graupel and hail embryos in high plains storms. *J. Atmos. Sci.*, **39**, 2867–2897, doi:10.1175/1520-0469(1982)039<2867:ACSOTR>2.0.CO;2.

——, and C. D. Westbrook, 2010: Advances in the estimation of ice particle fall speeds using laboratory and field measurements. *J. Atmos. Sci.*, **67**, 2469–2482, doi:10.1175/2010JAS3379.1.

——, A. Bansemer, C. Schmitt, C. Twohy, and M. Poellot, 2004: Effective ice particle densities derived from aircraft data. *J. Atmos. Sci.*, **61**, 982–1003, doi:10.1175/1520-0469(2004)061<0982:EIPDDF>2.0.CO;2.

Huang, G.-J., V. N. Bringi, R. Cifelli, D. Hudak, and W. A. Petersen, 2010: A methodology to derive radar reflectivity–liquid equivalent snow rate relations using C-band radar and a 2D video disdrometer. *J. Atmos. Oceanic Technol.*, **27**, 637–651, doi:10.1175/2009JTECHA1284.1.

——, ——, D. Moisseev, W. A. Petersen, L. Bliven, and D. Hudak, 2015: Use of 2D-video disdrometer to derive mean density–size and Z_e–SR relations: Four snow cases from the light precipitation validation experiment. *Atmos. Res.*, **153**, 34–48, doi:10.1016/j.atmosres.2014.07.013.

Kajikawa, M., 1972: Measurement of falling velocity of individual snow crystals. *J. Meteor. Soc. Japan*, **50**, 276–283.

Kennedy, P., and S. Rutledge, 2011: S-band dual-polarization radar observations of winter storms. *J. Appl. Meteor. Climatol.*, **50**, 844–858, doi:10.1175/2010JAMC2558.1.

Khvorostyanov, V., and J. A. Curry, 2002: Terminal velocities of droplets and crystals: Power laws with continuous parameters over the size spectrum. *J. Atmos. Sci.*, **59**, 1872–1884, doi:10.1175/1520-0469(2002)059<1872:TVODAC>2.0.CO;2.

——, and ——, 2005: Fall velocities of hydrometeors in the atmosphere: Refinements to a continuous analytical power law. *J. Atmos. Sci.*, **62**, 4343–4357, doi:10.1175/JAS3622.1.

Kneifel, S., A. von Lerber, J. Tiira, D. Moisseev, P. Kollias, and J. Leinonen, 2015: Observed relations between snowfall microphysics and triple-frequency radar measurements. *J. Geophys. Res. Atmos.*, **120**, 6034–6055, doi:10.1002/2015JD023156.

Kruger, A., and W. Krajewski, 2002: Two-dimensional video disdrometer: A description. *J. Atmos. Oceanic Technol.*, **19**, 602–617, doi:10.1175/1520-0426(2002)019<0602:TDVDAD>2.0.CO;2.

Kyrouac, J., and D. Holdridge, 2014: ARM Surface Meteorological Instrumentation (MET). Atmospheric Radiation Measurement (ARM) Climate Research Facility Data Archive, Oak Ridge, TN, accessed 11 April 2014, doi:10.5439/1025220.

Lakshmanan, V., J. Zhang, K. Hondl, and C. Langston, 2012: A statistical approach to mitigating persistent clutter in radar reflectivity data. *IEEE J. Sel. Top. Appl. Earth Obs. Remote Sens.*, **5**, 652–662, doi:10.1109/JSTARS.2011.2181828.

Langille, R. C., and R. S. Thain, 1951: Some quantitative measurements of three-centimeter radar echoes from falling snow. *Can. J. Phys.*, **29**, 482–490, doi:10.1139/p51-052.

Langleben, M. P., 1954: The terminal velocity of snowflakes. *Quart. J. Roy. Meteor. Soc.*, **80**, 640–642, doi:10.1002/qj.49708034619.

Lee, G., and I. Zawadzki, 2005: Variability of drop size distributions: Noise and noise filtering in disdrometric data. *J. Appl. Meteor.*, **44**, 634–652, doi:10.1175/JAM2222.1.

Leinonen, J., D. Moisseev, M. Leskinen, and W. Petersen, 2012: A climatology of five-year disdrometer observations of rainfall in Finland with implications for global radar observations. *J. Appl. Meteor. Climatol.*, **51**, 392–404, doi:10.1175/JAMC-D-11-056.1.

Lim, S., D. Moisseev, V. Chandrasekar, and D.-R. Lee, 2013: Classification and quantification of snow based on spatial variability of radar reflectivity. *J. Meteor. Soc. Japan Ser. II*, **91**, 763–774, doi:10.2151/jmsj.2013-603.

List, R., and R. Schemenauer, 1971: Free-fall behavior of planar snow crystals, conical graupel and small hail. *J. Atmos. Sci.*, **28**, 110–115, doi:10.1175/1520-0469(1971)028<0110:FFBOPS>2.0.CO;2.

Locatelli, J., and P. Hobbs, 1974: Fall speeds and masses of solid precipitation particles. *J. Geophys. Res.*, **79**, 2185–2197, doi:10.1029/JC079i015p02185.

Löffler-Mang, M., and J. Joss, 2000: An optical disdrometer for measuring size and velocity of hydrometeors. *J. Atmos. Oceanic Technol.*, **17**, 130–139, doi:10.1175/1520-0426(2000)017<0130:AODFMS>2.0.CO;2.

——, and U. Blahak, 2001: Estimation of the equivalent radar reflectivity factor from measured snow size spectra. *J. Appl. Meteor.*, **40**, 843–849, doi:10.1175/1520-0450(2001)040<0843:EOTERR>2.0.CO;2.

Magono, C., and T. Nakamura, 1965: Aerodynamic studies of falling snowflakes. *J. Meteor. Soc. Japan*, **43**, 139–147.

Marshall, J. S., and K. L. S. Gunn, 1952: Measurement of snow parameters by radar. *J. Meteor.*, **9**, 322–327, doi:10.1175/1520-0469(1952)009<0322:MOSPBR>2.0.CO;2.

Matrosov, S., R. Reinking, and I. Djalalova, 2005: Inferring fall attitudes of pristine dendritic crystals from polarimetric radar data. *J. Atmos. Sci.*, **62**, 241–250, doi:10.1175/JAS-3356.1.

Mitchell, D. L., 1996: Use of mass- and area-dimensional power laws for determining precipitation particle terminal velocities. *J. Atmos. Sci.*, **53**, 1710–1723, doi:10.1175/1520-0469(1996)053<1710:UOMAAD>2.0.CO;2.

——, and A. J. Heymsfield, 2005: Refinements in the treatment of ice particle terminal velocities, highlighting aggregates. *J. Atmos. Sci.*, **62**, 1637–1644, doi:10.1175/JAS3413.1.

——, R. Zhang, and R. L. Pitter, 1990: Mass-dimensional relationships for ice particles and the influence of riming on snowfall rates. *J. Appl. Meteor.*, **29**, 153–163, doi:10.1175/1520-0450(1990)029<0153:MDRFIP>2.0.CO;2.

Moisseev, D. N., S. Lautaportti, J. Tyynela, and S. Lim, 2015: Dual-polarization radar signatures in snowstorms: Role of snowflake aggregation. *J. Geophys. Res. Atmos.*, **120**, 12 644–12 655, doi:10.1002/2015JD023884.

Morrison, H., and J. Milbrandt, 2015: Parameterization of cloud microphysics based on the prediction of bulk ice particle properties. Part I: Scheme description and idealized tests. *J. Atmos. Sci.*, **72**, 287–311, doi:10.1175/JAS-D-14-0065.1.

Muramoto, K.-I., K. Matsuura, and T. Shiina, 1995: Measuring the density of snow particles and snowfall rate. *Electron. Commun. Japan Part III*, **78**, 71–79, doi:10.1002/ecjc.4430781107.

Nakaya, U., and T. Tereda, 1935: Simultaneous observations of the mass, falling velocity and form of individual snow crystals. *J. Fac. Sci. Hokkaido Univ. Ser. 7*, **1**, 191–200.

Nešpor, V., W. F. Krajewski, and A. Kruger, 2000: Wind-induced error of raindrop size distribution measurement using a two-dimensional video disdrometer. *J. Atmos. Oceanic Technol.*, **17**, 1483–1492, doi:10.1175/1520-0426(2000)017<1483:WIEORS>2.0.CO;2.

Newman, A. J., P. A. Kucera, and L. F. Bliven, 2009: Presenting the Snowflake Video Imager (SVI). *J. Atmos. Oceanic Technol.*, **26**, 167–179, doi:10.1175/2008JTECHA1148.1.

Ohtake, T., and T. Hemni, 1970: Radar reflectivity on aggregated snowflakes. Preprints, *14th Conf. on Radar Meteorology*, Tucson, AZ, Amer. Meteor. Soc., 209–210.

Petäjä, T., and Coauthors, 2016: BAECC: A field campaign to elucidate the impact of biogenic aerosols on clouds and climate. *Bull. Amer. Meteor. Soc.*, **97**, 1909–1928, doi:10.1175/BAMS-D-14-00199.1.

Petras, I., and D. Bednarova, 2010: Total least squares approach to modeling: A Matlab toolbox. *Acta Montan. Slovaca*, **15**, 158–170.

Pruppacher, H., and J. Klett, 1997: *Microphysics of Clouds and Precipitation*. Kluwer Academic, 954 pp.

Puhakka, T., 1975: On the dependence of the *Z–R* relation on the temperature in snowfall. Preprints, *16th Conf. on Radar Meteorology*, Houston, TX, Amer. Meteor. Soc., 504–507.

Rasmussen, R., M. Dixon, S. Vasiloff, F. Hage, S. Knight, J. Vivekanandan, and M. Xu, 2003: Snow nowcasting using a real-time correlation of radar reflectivity with snow gauge accumulation. *J. Appl. Meteor.*, **42**, 20–36, doi:10.1175/1520-0450(2003)042<0020:SNUART>2.0.CO;2.

——, and Coauthors, 2012: How well are we measuring snow: The NOAA/FAA/NCAR winter precipitation test bed. *Bull. Amer. Meteor. Soc.*, **93**, 811–829, doi:10.1175/BAMS-D-11-00052.1.

Saltikoff, E., A. Huuskonen, H. Hohti, J. Koistinen, and H. Järvinen, 2010: Quality assurance in the FMI Doppler weather radar network. *Boreal Environ. Res.*, **15**, 579–594.

Schmitt, C., and A. Heymsfield, 2010: The dimensional characteristics of ice crystal aggregates from fractal geometry. *J. Atmos. Sci.*, **67**, 1605–1616, doi:10.1175/2009JAS3187.1.

Schönhuber, M., G. Lammer, and W. Randeu, 2007: One decade of imaging precipitation measurement by 2D-video-distrometer. *Adv. Geosci.*, **10**, 85–90, doi:10.5194/adgeo-10-85-2007.

Sekhon, R. S., and R. C. Srivastava, 1970: Snow size spectra and radar reflectivity. *J. Atmos. Sci.*, **27**, 299–307, doi:10.1175/1520-0469(1970)027<0299:SSSARR>2.0.CO;2.

Sihvola, A., 1999: *Electromagnetic Mixing Formulas and Applications*. Institution of Electrical Engineers, 284 pp.

Skofronick-Jackson, G., B. Johnson, and S. Munchak, 2013: Detection thresholds of falling snow from satellite-borne active and passive sensors. *IEEE Trans. Geosci. Remote Sens.*, **51**, 4177–4189, doi:10.1109/TGRS.2012.2227763.

Smith, P., 1984: Equivalent radar reflectivity factors for snow and ice particles. *J. Climate Appl. Meteor.*, **23**, 1258–1260, doi:10.1175/1520-0450(1984)023<1258:ERRFFS>2.0.CO;2.

——, and D. Kliche, 2005: The bias in moment estimators for parameters of drop size distribution functions: Sampling from exponential distributions. *J. Appl. Meteor.*, **44**, 1195–1205, doi:10.1175/JAM2258.1.

Szyrmer, W., and I. Zawadzki, 2010: Snow studies. Part II: Average relationship between mass of snowflakes and their terminal fall velocity. *J. Atmos. Sci.*, **67**, 3319–3335, doi:10.1175/2010JAS3390.1.

Thompson, E. J., S. A. Rutledge, B. Dolan, V. Chandrasekar, and B. L. Cheong, 2014: A dual-polarization radar hydrometeor classification algorithm for winter precipitation. *J. Atmos. Oceanic Technol.*, **31**, 1457–1481, doi:10.1175/JTECH-D-13-00119.1.

Thompson, G., R. Rasmussen, and K. Manning, 2004: Explicit forecasts of winter precipitation using an improved bulk microphysics scheme. Part I: Description and sensitivity analysis. *Mon. Wea. Rev.*, **132**, 519–542, doi:10.1175/1520-0493(2004)132<0519:EFOWPU>2.0.CO;2.

Tiira, J., D. N. Moisseev, A. von Lerber, D. Ori, A. Tokay, L. F. Bliven, and W. Petersen, 2016: Ensemble mean density and its connection to other microphysical properties of falling snow as observed in southern Finland. *Atmos. Meas. Tech.*, **9**, 4825–4841, doi:10.5194/amt-9-4825-2016.

Turk, F., K.-W. Park, Z. Haddad, P. Rodriguez, and D. Hudak, 2011: Constraining *CloudSat*-based snowfall profiles using surface observations and C-band ground radar. *J. Geophys. Res.*, **116**, D23205, doi:10.1029/2011JD016126.

Wood, N. B., T. S. L'Ecuyer, F. Bliven, and G. Stephens, 2013: Characterization of video disdrometer uncertainties and impacts on estimates of snowfall rate and radar reflectivity. *Atmos. Meas. Tech.*, **6**, 3635–3648, doi:10.5194/amt-6-3635-2013.

——, ——, A. J. Heymsfield, G. L. Stephens, D. R. Hudak, and P. Rodriguez, 2014: Estimating snow microphysical properties using collocated multisensor observations. *J. Geophys. Res. Atmos.*, **119**, 8941–8961, doi:10.1002/2013JD021303.

——, ——, ——, and ——, 2015: Microphysical constraints on millimeter-wavelength scattering properties of snow particles. *J. Appl. Meteor. Climatol.*, **54**, 909–931, doi:10.1175/JAMC-D-14-0137.1.

Zikmunda, J., 1972: Fall velocities of spatial crystals and aggregates. *J. Atmos. Sci.*, **29**, 1511–1515, doi:10.1175/1520-0469(1972)029<1511:FVOSCA>2.0.CO;2.

——, and G. Vali, 1972: Fall patterns and fall velocities of rimed ice crystals. *J. Atmos. Sci.*, **29**, 1334–1347, doi:10.1175/1520-0469(1972)029<1334:FPAFVO>2.0.CO;2.